
Estimating optical vegetation indices with Sentinel-1 SAR data and AutoML

Daniel Paluba¹, Bertrand Le Saux², Francesco Sarti³, Přemysl Stych¹

¹ Department of Applied Geoinformatics and Cartography, Faculty of Science, Charles University, Prague, Czechia; contact: palubad@natur.cuni.cz, stych@natur.cuni.cz

² Φ-lab - Climate Action, Sustainability and Science Department (EOP-S) Department, Earth Observation Programmes Directorate, European Space Agency (ESA/ESRIN), Frascati, Italy

³ Earth Observation Programmes Directorate, European Space Agency (ESA/ESRIN), Frascati, Italy

Abstract

Current optical vegetation indices (VIs) for monitoring forest ecosystems are well established and widely used in various applications. However, continuous monitoring of vegetation based on optical satellite data can be hampered by atmospheric effects such as clouds. On the contrary, synthetic aperture radar (SAR) data can offer insightful and systematic forest monitoring with complete time series due to signal penetration through clouds and day and night image acquisitions. The goal of this work is to overcome the issues affecting optical data with SAR data and serve as a substitute for estimating optical VIs for forests using machine learning. Time series of four VIs (LAI, FAPAR, EVI and NDVI) were estimated using multitemporal Sentinel-1 SAR and ancillary data. Both healthy and disturbed forest areas in 2021 in Czechia were used, while labels (“ground truth”) were generated from Sentinel-2 multispectral data. This was enabled by creating a paired multi-temporal and multi-modal dataset in Google Earth Engine (GEE), including temporally and spatially aligned Sentinel-1, Sentinel-2, DEM, weather and land cover datasets (MMT-GEE). The performance of a Random Forest Regression, as a baseline algorithm, was compared to a performance of an open-source Automatic Machine Learning (AutoML) approach, the auto-sklearn, for each VI. The use of ancillary features generated from DEM improved the results, while the inclusion of additional weather information further improved the results. Auto-sklearn outperformed RFR for three out of four VIs, while a 1-hour optimization length was enough to achieve sufficient results with an R^2 of 69-84% with low errors (0.05-0.32 of MAE depending on VI). Moreover, great agreement was found for selected case studies in the time series analysis and in the spatial comparison between the original and estimated SAR-based VIs. In general, compared to VIs from currently freely available optical satellite data and available global VI products, a better temporal resolution (up to 240 measurements / year) and a better spatial resolution (20 m) were achieved using estimated SAR-based VIs with high accuracy. A great advantage of the SAR-based VI is the ability to detect abrupt forest changes with a sub-weekly temporal accuracy.

Keywords: SAR, Sentinel-1, vegetation index, forest, AutoML, machine learning

Introduction

Covering about 30% of the Earth's surface (Hansen et al. 2013), forest plays an inevitable role in the preservation of biodiversity, regulating global and regional carbon cycles (Pan et al. 2011; McMahon, Parker, and Miller 2010). Forest ecosystems have been dynamically changing on Earth, influenced by several anthropogenic and natural factors. Forest change is an important ecological process leading to reestablishment of forest biomass and structure (Bartels et al. 2016) (Bartels et al., 2016). Nowadays, in the era of big data and cloud-computing platforms, remote sensing (RS) data and techniques have become an essential part of forest monitoring from a local to global scale. RS data and techniques enable us to monitor the dynamics of large-scale forest ecosystems in a systematic way and almost in a near-real time. Recent studies have proven a key role of RS in monitoring changes in European temperate forests caused by various natural disturbances, such as bark beetle calamities (Hlásny et al. 2021; Lastovicka et al. 2020; Stych et al. 2019), windthrows (Dalponte et al. 2020; Baumann et al. 2014), wildfires (Quintano, Fernández-Manso, and Fernández-Manso 2018; García-Llamas et al. 2019) or drought (Schellenberg et al. 2023; Kaiser et al. 2022), but also forest regeneration and regrowth.

Traditionally, optical vegetation indices (VIs) have been found to be effective in monitoring forest health condition, its phenology phases. The most widely-used parameters for vegetation monitoring are the Normalized Difference Vegetation Index (NDVI), Enhanced Vegetation Index (EVI), Leaf Area Index (LAI) and the Fraction of Absorbed Photosynthetically Active Radiation (FAPAR). NDVI is the most popular VI due to its simplicity, long history, and the fact that it can be created from the data of almost every RS sensor (Huang et al. 2021). EVI has an improved sensitivity in high biomass regions compared to NDVI and it reduces the influence of the ground and atmosphere signal on the canopy response (Huete et al. 2002). LAI and FAPAR were identified as terrestrial Essential Climate Variables (ECV) by the Global Climate Observing System (WMO et al. 2011). These VIs are generated also on the global scale, e.g. NDVI and EVI from the MODIS or from NASA Visible Infrared Imaging Radiometer Suite (VIIRS) (at 250-1000 m and 16 days of spatial and temporal resolution, respectively) (Didan 2021b; 2021a; Didan and Barreto 2018), LAI and FPAR from MODIS and VIIRS (500 m and 4-8 days) (Myneni, Knyazikhin, and Park 2021; Myneni and Knyazikhin 2018), NDVI, LAI and FAPAR from the Copernicus Global Land Service (CGLS) (300 m and 10 days) (Fuster et al. 2020) or the pan-european Sentinel-2 LAI, FAPAR and NDVI products (10 m 1 day) (Smets et al. 2023). However, the real temporal resolution of these products depends on the availability of cloud-free acquisitions. In general, optical VIs are also prone to atmospheric effects, which can make even cloud-free measurements incomparable.

On the other hand, Synthetic Aperture Radar (SAR) data which are prone to clouds and atmospheric effects and with daylight-independence can not only overcome the problems that affect optical data, but can also serve as a substitute in order to estimate the values of data gaps in optical RS. SAR data have been utilized to monitor deforestation and forest degradation in tropical areas (Reiche et al. 2021), bark beetle calamities (Marinelli et al. 2023), wildfire progression (Ban et al. 2020; Paluba et al. 2023), windthrow detection (Rüetschi, Small, and Waser 2019; Dalponte et al. 2023) or seasonal variation monitoring (Dostalova et al. 2016; Dostálová et al. 2018). In recent years, SAR polarimetric indices were developed for vegetation monitoring based on backscatter coefficient, e.g. co-polarization ratios (PR) of VH/VV or VV/VH, Radar Vegetation Index (RVI), Radar Forest Degradation Index (RFDI), polarimetric radar vegetation index (PRVI), dual polarimetric SAR vegetation index (DPSVI) (Frison et al. 2018; Chang, Shoshany, and Oh 2018; Alvarez-Mozos et al. 2021; Hird et al. 2017; Kim and van Zyl 2000; Periasamy 2018; dos Santos, Da Silva, and do Amaral 2021) or incorporating also the phase information, e.g. the Dual-pol radar vegetation index (DpRVI) or the Compact-pol RVI (CpRVI) (Mandal, Kumar, et al. 2020; Mandal, Ratha, et al. 2020). Moreover, the relationship between optical and SAR features was found to be significant in previous studies. Moderate to high correlations were found between NDVI and SAR polarizations (VH and VV) and polarimetric indices (Radar Vegetation Index - RVI, VH/VV, VV/VH and other) for crop monitoring, e.g. in (Alvarez-Mozos et al. 2021; Filgueiras et al. 2019; Holtgrave et al. 2020; Jiao, McNairn, and Dingle Robertson 2021; Moran et al. 2012). However, these analyzes were performed on an image-by-image basis and no time series data were included. A strong correlation between NDVI and the co-polarimetric ratio VH/VV for forest time series was also found in (Frison et al. 2018).

Based on the relationship found between optical and SAR polarizations and indices, some researchers tried to estimate optical VIs using SAR data and machine learning (ML) methods. In (Filgueiras et al. 2019), 8 different regression algorithms were tested to estimate the NDVI for crop monitoring, from which the random forest (RF) regressor performed the best with a mean absolute error (MAE) of 0.034-0.075 and a Root Mean Square Error (RMSE) of 0.020-0.037. Next to NDVI, estimation of EVI with ML was tested in (dos Santos et al. 2022), while finding the RF as the best performing regressor. RF as a best performing algorithm was found in (Lasko 2022) and (Mohite et al. 2020) for filling data gaps in NDVI images using SAR data and for NDVI prediction from SAR data for agricultural crops. In these works, tabular regression was used. More advanced methods using image patches in a deep learning approach were used, e.g. in (Roßberg and Schmitt 2022) and (Roßberg and Schmitt 2023). They estimated NDVI for different land cover types globally using a U-net architecture with 2300 temporally and spatially paired S1 and S2 image patches, achieving an MAE of 0.1. In (Calota, Faur, and Datcu 2022), the bag-of-words method in a three-layered and VGG-19 CNN was used to estimate the NDVI values from SAR data using BigEarthNet image patches. CNN to predict NDVI values was used in (Mazza et al. 2018), who found that fusing temporally adjacent SAR images and adding a speckle filter improves accuracy.

Nowadays, when there is a rapid increase of new ML algorithms (Tuia et al. 2023; 2017), it can be difficult to decide which algorithms to include in the comparison and how to find the best performing ML pipeline for a specific task. Automatic Machine Learning (AutoML) approaches are out-of-the-box ML methods which are aimed at finding the best performing ML pipelines, selecting the best data and feature preprocessing methods, the best algorithms and their hyperparameters, and creating an ensemble of the best models. All of this is performed using an optimizer, such as a Bayesian optimizer, to boost the optimizations by learning from previous steps. It can use meta-learning, i.e. learning from similar datasets from the past. Therefore, AutoML can automate the repetitive process of finding the best ML pipeline and it also lowers the barrier to create high-performing models for less experienced users in ML. The RS community gained interest in various AutoML frameworks, such as auto-sklearn (Feurer et al. 2015), Tree-based Pipeline Optimization Tool (TPOT) (Olson and Moore 2019) or AutoGluon (Erickson et al. 2020) for tabular-based tasks or Auto-Keras (Jin et al. 2023) for image-based tasks, e.g. deep learning classification. Current RS-oriented works using AutoML frameworks present various applications, e.g. for preparation of an AutoML classification design for RS data (Palacios Salinas et al. 2021) using Auto-Keras, for classification of a tropical landscape using Sentinel-2 and Landsat 8 data using the TPOT framework in (Kiala et al. 2020), for identification of weeds in (Espejo-Garcia et al. 2021) using AutoKeras and Auto-sklearn frameworks, landslide susceptibility with Sentinel-2 data with Auto-Keras in (Renza et al. 2021). For regression tasks, AutoML was used for tomato yield prediction with Sentinel-2 data using auto-sklearn in (Darra et al. 2023), for modeling forest aboveground biomass predictions with Sentinel-2 data in (Naik, Dalponte, and Bruzzone 2023), for estimating grass height using Landsat data in (César de Sá et al. 2022) by comparing auto-sklearn and AutoGluon, predicting grape sugar content with auto-sklearn in (Kasimati et al. 2022). Auto-sklearn is therefore one of the most used AutoML frameworks in general, but also in RS. It is open-source and is completely built on the popular scikit-learn Python library (Pedregosa et al. 2011). Furthermore, in benchmark tests, auto-sklearn outperformed other popular AutoML frameworks for both classification in (Feurer et al. 2015) and (Feurer et al. 2022), and regression tasks in (Conrad et al. 2022), while better performance compared to AutoGluon was also achieved in a regression using RS data in (César de Sá et al. 2022).

The goal of this study is to estimate optical VI time series for forest monitoring using SAR and other ancillary data (e.g., elevation, weather conditions) with ML approaches. For this purpose, in the first step, a temporally and spatially paired dataset of S1, S2 and ancillary datasets with data preparation and preprocessing pipelines is developed in GEE. Two ML approaches are then compared, a traditional approach and an AutoML approach. The RFR was selected as a baseline algorithm, which is a well-performing ML algorithm for similar purposes. The RFR was compared to an AutoML approach, auto-sklearn with different lengths of optimization runs. The correlation between SAR features (polarizations, polarimetric indices) is assessed together with the evaluation of feature importance in regressions. The advantages and drawbacks of the methods used and the SAR and other ancillary data are discussed in the estimation of the time series of optical VIs.

Materials and Methods

Data

Only open-access data were used in this study. Copernicus Sentinel-1 SAR data (S1) and Sentinel-2 multispectral data (S2) operated by the European Space Agency (ESA) were used as main data sources for analysis and as validation / reference data, respectively. The Copernicus Sentinel-1 C-band (with 5.405 GHz central frequency) SAR data in Ground-range detected (GRD) were accessed from GEE with a pixel size of 10 m and a spatial resolution of about 20 x 22 m. Therefore, a spatial resolution of 20 m was used in the entire data processing in GEE and in further analyses. S1 data acquired before 2022 was used to explore the full potential of both Sentinel-1A and B satellites, which provided a 6-day temporal resolution until the end of 2021 when an anomaly happened to the Sentinel-1B satellite (Pinheiro et al. 2022). The S2 mission with its two sun-synchronously orbiting satellites provides images of the Earth's surface in the optical domain every 5 days in a spatial resolution of 10, 20 and 60 m, depending on wavelength.

To improve performance, other ancillary data were also assessed and used: the Copernicus DEM digital elevation model (COP-DEM) and weather data from the ERA-5 Land mission. Elevation models provide useful information on the suitability of the local ecosystem for trees and have a proven record of improving ML algorithms (Carvalho et al. 2020; Hänsch et al. 2022). The COP-DEM (European Space Agency and Airbus 2022) is a Digital Surface Model (DSM) representing the surface of the Earth, including buildings, infrastructure and vegetation for the time frame between 2011 and 2015. It is based on TanDEM-X satellite products provided by the German Aerospace Centre (DLR) and Airbus Defence and Space. In this work, the COP-DEM GLO-30 product was used, which represents a global DEM with a spatial resolution of 30 m. The COP-DEM was used to provide information on elevation, calculate slope, and local incidence angle (LIA). The LIA was calculated for each S1 image separately based on (Paluba et al. 2021).

The ERA5-land is a reanalysis dataset from the original ERA5 dataset with an hourly temporal resolution and with an enhanced resolution of 0.1 arc degrees with a native resolution of 9 km (Copernicus Climate Change Service 2019, 5). The dataset includes 50 variables in an hourly step from 1981, from which two variables were used: “temperature_2m” – an average temperature of air 2 meters above the surface; and “total_precipitation” – accumulated liquid and frozen water, including rain and snow, that falls to the Earth's surface. The following meteorological data were used from the ERA5 Land database for the selected study area: the sum of precipitation 12 hours prior to SAR acquisition, and temperature at the time of acquisition.

Three land cover databases, specifically ESA WorldCover v200 (ESA WC) for 2021 in a spatial resolution of 10 m (Zanaga et al. 2022), Corine Land Cover (CLC) for 2018 with a spatial resolution of 100 m and a minimal mapping unit of 25 ha (Kosztra et al. 2019), Copernicus Global Land Cover Layers Collection 3 (GLCL) (Buchhorn et al. 2020) with a spatial resolution of 10 m, and a forest-oriented database, the Hansen Global Forest Change v1.10 (GFC) with a spatial resolution of 30 m (Hansen et al. 2013) were used for forest mask generation.

In the first step, data was assessed and pre-processed in the GEE platform. Sentinel-1 and Sentinel-2 image collections were filtered to select each acquisition in 2021 for the study area, Czechia. Weather data were filtered just temporally, and DEM data was filtered just spatially.

Methods

The methodology in this work was divided into two main parts: 1) data preparation and preprocessing, and 2) data exploration analysis and forest parameter estimation with ML. In the first step, the multi-modal and multi-temporal dataset in GEE (MMT-GEE) is developed. First, forest masks of coniferous and broad-leaved forests, as well as forest loss areas, were created for Czechia using an intersection of four different forest and land cover databases. Random points (with a 20 m buffer) were generated for each class and validated using high-resolution aerial photos in Google Earth Pro. After the validation, 600 areas were selected for each class. After accessing the entire S1 and S2 image collections in GEE over Czechia in 2021, a pre-processing was applied to each image separately and a paired S1-S2 image collection was created based on their temporal and

spatial overlay. Furthermore, other ancillary data were generated using DEM and weather databases and added to each pair of S1-S2 images as additional image features. In the end, a feature extraction was performed on each S1-S2 image pair for each area and the data was exported from GEE. The data collection and preparation workflow can be seen in Figure 1, while each step is described in detail in the following sections.

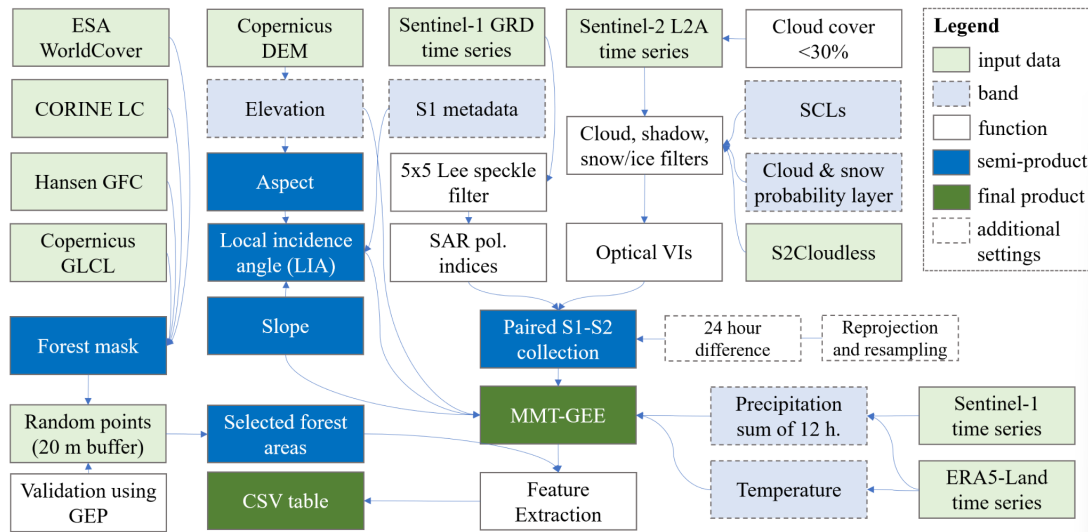


Fig. 1. Data pre-processing and preparation workflow in GEE.

In the second step, data preprocessing and subsequent data exploration analysis were performed on the exported dataset from GEE using pairwise correlation between the input features and permutation analysis using RFR. The importance of variance in the data by including disturbed forest areas was further explored using the RFR performance in case studies and RFR feature importance analysis. After that, the RFR was used to explore the importance of speckle filtering, as well as radiometric terrain correction. The RFR and the auto-sklearn AutoML library were tested to estimate optical VIs using SAR and ancillary data. Different combinations of input features were also tested. Auto-sklearn was tested for different lengths of the ML pipeline optimization (runs). The accuracy of the results was validated using the MAE and the root mean square error (RMSE) and R^2 , and a time series analysis, as well as spatial comparison was performed comparing the original S2 and the SAR-based VIs. All these steps are described in detail in the following sections.

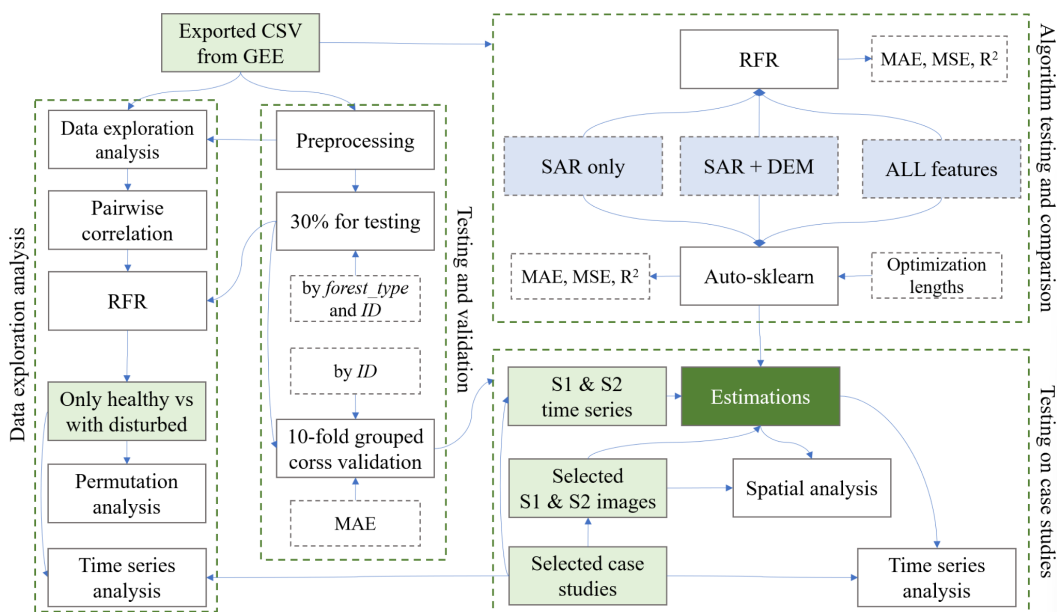


Figure 2. Data analysis workflow.

Data Preparation and Pre-Processing in GEE, and the MMT-GEE Dataset

Study Areas

Coniferous and broad-leaved forest areas in Czechia were selected for this study. In 2021, forests represented 34% of the total area of Czechia (Ministry of Agriculture of the Czech Republic 2022). Coniferous species represented 70% of all forest cover, while the most populous are Norway Spruce (68% of all conifers), followed by pines (23%) and larch (6%). Broad-leaved species are represented mainly by beech (32% of all broad-leaved species), oak (27%) and birch (10%) (Ministry of Agriculture of the Czech Republic 2022).

Forest Mask Creation

Healthy forest masks were created based on an intersection of three land cover databases (ESA WC, CLC and GLCL) and a forest-oriented database (GFC). From the GFC database, only pixels of the base layer from 2000 with a canopy closure greater than 50% were selected. Pixels where a forest loss occurred between 2000 and 2021 (forest_loss band) were masked out. The CLC and GLCL databases allowed the differentiation between coniferous and broad-leaved forests; therefore, based on their intersect, broad-leaved and coniferous forest masks were created. Consequently, around 1200 random points with a 20 m buffer, entirely located inside the forest masks, were generated for the whole of Czechia for each forest type.

To introduce greater variation in the data, disturbed forest areas were also added. Forest masks for disturbed areas (disturbed forest masks), where pixels representing forest loss between 2018 and 2021 were selected. The differentiation between coniferous and broad-leaved forests was made based on an intersection of the loss mask, CLC from 2018 and GLCL from 2019, where these areas were classified as broad-leaved or coniferous forests. 50 000 random points with a 20 m buffer were generated in Czechia and only areas entirely covering the disturbed forest masks were selected.

Training and Testing Data Validation

In the next step, a validation of the automatically generated data (~1200 from each class) was performed to include only areas that in fact represent forested or non-forested areas. These areas with a 20 m buffer were validated using a visual analysis with Google Earth Pro high-resolution images (provided by CNES/Airbus and Maxar Technologies) to differentiate between broad-leaved and coniferous forests using images that capture both leaf-on (summer) and leaf-off (winter) conditions of the forests. However, one type of coniferous tree, the European Larch (*Larix decidua*), is characterized by losing its needles in autumn, and therefore it is classified as deciduous conifer. It can be easily recognized thanks to its cone-shaped crown (typical for conifers) and leaf-off state during winter time (typical for deciduous trees), therefore from high resolution imagery it was possible to identify these types. In the satellite time series, it would cause discrepancies between coniferous and broad-leaved forests, therefore, European larches were excluded from both the broad-leaved and coniferous database. Areas with at least 75% tree coverage by the selected forest types were considered valid and left in the database for further analysis. Areas located on the borders of different forest growth stages (e.g., small young versus high old pines) were excluded to avoid the effects of possible SAR shadowing on young trees caused by higher trees. Areas containing water or paved / concrete roads were also excluded. Forest loss in this work was defined as non-forest cover caused in 2021, where forest loss occurred in 2021. For these automatically generated forest loss data, data from 2021 and 2022 were used to validate the accuracy of this process. The differentiation between disturbed and healthy forests was usually straightforward for the reference years 2021 and 2022.

The final input dataset included 600 healthy coniferous, 600 healthy broad-leaved and 600 disturbed coniferous areas. Disturbed broad-leaved forest areas were excluded from the analysis, as only a few examples were found according to the requirements (40x40 m in area and disturbance occurred in 2021 according to the disturbed forest mask described in the previous section). The spatial distribution and terrain characteristics of the selected areas can be found in Fig. 3 and Table I, respectively.

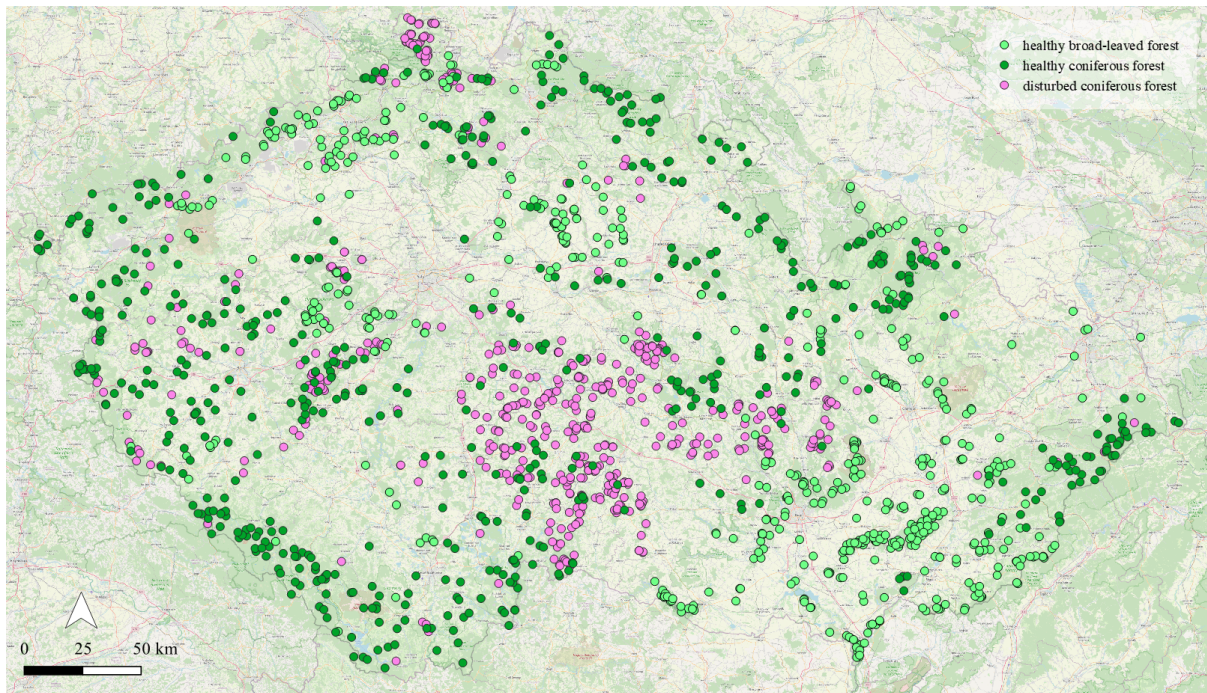


Fig. 3. Distribution of the forest areas used in this study.

Table I. Terrain-based characteristics of the forest areas

Input data type	Mean/median altitude in meters (Q1-Q3)	Mean/median slope in degrees (Q1-Q3)	Mean/median LIA in degrees (Q1/Q3)
Coniferous forests	650/643 (493-793)	10/8 (5-13)	39/39 (33-45)
Broad-leaved forests	417/406 (304-505)	12/11 (6-16)	38/39 (32-45)
Disturbed coniferous	580/587 (509-649)	9/8 (5-12)	38/38 (32-43)

Case Studies for Healthy and Disturbed Forest Time Series Analysis

Four case studies with a 40x40 m area were selected to compare optical VIs of the S2 time series and the estimated time series using SAR and ancillary data. For healthy case studies, a broad-leaved and a coniferous forest area was selected. To demonstrate the ability of the model to recognize and predict disturbed areas, one area where the disturbance occurred during the monitored time frame, i.e., in 2021, and one area where the disturbance occurred before 2021 were selected. General information, such as their X, Y coordinates of the center, tree cover composition, terrain characteristics and the number of available SAR acquisitions in 2021 can be found in Table II.

Table II. Characteristics of the selected case studies.

Forest type	X, Y coordinates of the center	Tree cover	elevation (m) / slope (°) / LIA range (°)	# SAR images
Broad-leaved	49.95776, 14.17296	100% tree cover	432 / 3 / 34-47	236
Coniferous	50.44805, 14.45740	100% tree cover	271 / 4 / 32-44	176
Disturbed coniferous during 2021	49.82402, 15.11192	100% tree cover to clear-cuts	552 / 9 / 23-48	232
Disturbed coniferous before 2021	49.35071, 15.51560	100% clear-cuts	641 / 4 / 30-39	175

Test area for spatial comparison of results

For visual comparison of the original and estimated VIs, a test area in the south-west of Czechia was selected, in the Krušné hory mountains. For this purpose, the NDVI was selected. The selected area represents a

complex mountainous terrain with a mean elevation of 742 m above sea level and mean slopes of 13°. It has almost the same representation of coniferous and broad-leaved forests (45 to 55% share) and contains around 28,000 forest pixels of 20 m spatial resolution (around 11 km²). The S2 optical and S1 SAR acquisitions are from the same day (8th September) with a temporal difference of 7 hours. This area was selected to represent mostly forest areas, where forest types differentiation and non-forest area masking was performed using the Copernicus High Resolution Layers (HRL) (Langanke 2017). Characteristics of the test area can be found in Table III.

Table III. Characteristics of the test area. C stands for coniferous forests, B stands for broad-leaved forests.

Name	Forest pixels (in thousands)	Forest type (C / B) in %	mean elevation (m) / slope (°) / LIA (°)	Date and time of S2 and S1 acquisitions
Krušné hory test area	28	45 / 55	742 / 13.0 / 35.1	S2: 08/09/2021 10AM S1: 08/09/2021 5PM

Data Pre-Processing and Feature Creation

To filter out as many areas covered by clouds, their shadows or snow cover in Sentinel-2 data as possible, image tiles with cloud cover higher than 30% were filtered out, and further three different methods for their masking were implemented. These methods included the S2Cloudless methodology (Zupanc 2017), masks created using the additional S2 L2A image bands, specifically the Scene Classification Layer band (*SCL*, values 1-3 and 7-10), and cloud (*MSK_CLDPRB*) and snow probability (*MSK_SNOWPRB*) bitmasks where the probability was higher than 5%. After that, the target VIs, specifically the LAI, FAPAR, NDVI and EVI, were calculated (Table IV).

Table IV. Target optical vegetation indices.

Optical VI	Formula	Source
NDVI	$\frac{NIR - RED}{NIR + RED}$	(Gamon et al. 1995)
EVI	$2.5 * \frac{NIR - RED}{NIR + 6*RED - 7.5*BLUE + 1}$	(Liu and Huete 1995)
LAI	<i>based on (Weiss and Baret 2016)</i>	GEE implementation by (Van Tricht 2023)
FAPAR	<i>based on (Weiss and Baret 2016)</i>	GEE implementation by (Van Tricht 2023)

For Sentinel-1 data, based on (Filgueiras et al. 2019), the Lee speckle filter with a window size of 5x5 pixels was applied to the S1 data. The Lee filter is one of the most used speckle filters, it is computationally efficient while effectively smoothing the speckle effect and preserving the edges or subtle details (Lee 1985). The polarimetric indices (VV/VH, VH/VV, Radar Forest Degradation Index - RFDI, Radar Vegetation Index - RVI, Dual Polarized SAR Vegetation Index - DPSVI and its normalized DPSVI_n and modified versions DPSVI_m) were then calculated in power units and added to enlarge the feature space (Table V). The VV and VH polarizations were converted to decibels (dB), to a logarithmic scale. The ancillary features (DEM and weather data) were calculated for each pixel of the image and added to the feature space.

Creating the MMT-GEE Dataset

After data pre-processing, an image collection including spatially and temporally joined S1 and S2 images, terrain characteristics (elevation, slope, LIA) and weather data (temperature, precipitation) is created. The joined S1-S2 image collection was created based on a spatial overlap and the 24 hour temporal difference between the pre-processed S1 and S2 acquisitions. The S1 images served as master images in image stacking, i.e. the S2 images were joined to the S1 images. The final image collection included the selected optical VIs, each SAR feature and each above-mentioned ancillary DEM and weather feature for a S1-S2 image combination. The dataset was resampled into a 20 meter grid, while reprojection and resampling in GEE are done automatically on-the-fly.

Table V. Used SAR polarimetric features. *in Alvarez et al. (2021) it was called the Normalized Difference Polarization Index (NDPI).

Name	Abbreviation	Formula	Source
Radar Vegetation Index	RVI	$4 * \frac{VH}{VH + VV}$	[1,2]
Radar Forest Degradation Index*	RFDI	$\frac{VV+VH}{VV - VH}$	[3]
Polarimetric Ratio 1	VV/VH	$\frac{VV}{VH}$	[4]
Polarimetric Ratio 2	VH/VV	$\frac{VH}{VV}$	[5]
Normalized Ratio Procedure between Bands	NRPB	$\frac{VH-VV}{VH + VV}$	[6]
Dual Polarized SAR Vegetation Index, original	DPSVI _o	$VH * \frac{VV_{max} * VH - VV * VH + VH^2}{1.414213562373095 * VV}$	[7]
Dual Polarized SAR Vegetation Index, modified	DPSVI _m	$\frac{VV_{max} - VV + VH}{1.414213562373095 * ((VV+VH)/VV) * VH}$	[8]
Dual Polarized SAR Vegetation Index, normalized	DPSVI _n	$VH * \frac{VV^2 + VV * VH}{1.414213562373095}$	[8]

References: [1]: (Kim and van Zyl 2000), [2]: (Sahadevan, Sitiraju, and Sharma 2013), [3]: (Saatchi 2019), [4]: (Frison et al. 2018), [5]: (Alvarez-Mozos et al. 2021), [6]: (Hird et al. 2017), [7]: (Periasamy 2018), [8]: (dos Santos, Da Silva, and do Amaral 2021)

Data Export from GEE

Healthy and disturbed forest areas were used to extract values from each S1-S2 combination. Each forest area had its unique ID and the date of SAR image acquisition. As the final step in GEE, each timestep-area combination including values of optical, SAR and ancillary features were exported from GEE in a csv table. The analysis was carried out using the original S1 coordinate system for Czechia (EPSG:32634) and with a spatial resolution of 20 meters, which matches the spatial resolution of the S1 data.

Data Exploration Analysis and Forest Parameter Estimation with ML

Data Exploration and Pairwise Correlation Analysis of Input Features

In the very first step, data exploration was performed. The size of the dataset for different days of the year (DOY) for coniferous, broad-leaved and disturbed coniferous forest areas was examined separately to assess the availability of data for different parts of the year. To gain insights into seasonality in the optical and SAR domain for each class, time series analysis was performed using all data (600 for each class) while also calculating the mean of the time series for each class. From the optical domain, the NDVI and LAI were selected, whereas for the SAR domain, the VV and VH time series were analyzed for each studied class.

In the next step, a pairwise correlation analysis was performed between input features considered for further analysis to assess similarities between them and to reduce possible data redundancy by excluding features. The second correlation analysis focused on exploring the relationship between SAR features and labels, i.e., optical VIs generated from S2 data. For these analyses, all exported data were used, i.e., each time step for each selected point. Pairwise correlation analysis was performed and a Pearson's correlation coefficient (r) was calculated on each combination of input features.

Random Forest Regression

The Random Forest Regressor (RFR) was selected as a baseline algorithm based on its best performance for VI estimations or optical data gap filling using SAR data in (Filgueiras et al. 2019; dos Santos et al. 2022; Lasko 2022; Mohite et al. 2020) and also due to its one of the best performances on 140 datasets for classification compared to other classifiers and auto-sklearn in (Feurer et al. 2015). The RF is one of the most used machine learning algorithms for classification and regression tasks in RS and it operates as an ensemble of decision trees, where each tree is constructed using randomly selected subsets of training data and features

(Belgiu and Drăguț 2016). The RFR model was retained with the original parameters from the scikit-learn Python library, that is, $n_estimators$ (number of trees) = 100, $criterion$ = 'squared error', $min_samples_split$ (the minimum number of samples required to split an internal node) = 2. Further details on additional parameters can be found in the documentation of scikit-learn, version 1.3.0 (scikit-learn 2023).

To underscore the importance of variance in data variability when estimating optical VIs using a combination of SAR and ancillary features, the RFR was used to estimate NDVI using data only from healthy forest areas. This analysis included an assessment of feature importance and the temporal behavior of the time series data for both healthy and disturbed case studies. In a subsequent step, forest areas that experienced disturbances in 2021 were introduced into the training and validation datasets. Once again, the feature importance and the behavior of the time series were assessed and subsequently compared with the state observed before the inclusion of disturbed areas.

Data Pre-Processing in Python

Preliminary data processing was performed prior to any analysis. Records which included null/ missing values were excluded from the analysis, therefore only records having values in each feature were included in the further pre-processing and analysis. The acquisition dates were transformed into DOY and then further transformed into cyclical sine and cosine features to ensure the proximity of values obtained in January to those obtained in December. In the next step, the data types were defined (categorical, numerical) and if needed, the values were casted to a lower numerical data type (e.g. Float16 instead of Float64) to speed up the following analysis.

Training, Validation and Testing

The three types of input datasets (healthy for both broad-leaved and coniferous forests and disturbed coniferous forests) were divided into training and testing datasets, while 30% of the data was selected as testing data. This division was done separately for each type of input dataset, while the division was also based on the requirement that records from the same area (with the same *ID*) could be included in either the training or testing dataset. The resulting training and testing datasets were merged. During the merging process, a new categorical feature, called "forest_type", was added, which specifically distinguishes only between broad-leaved and coniferous forests. This is important because broad-leaved and coniferous forests have different phenological responses/seasonality over the year and it is also detectable using time series of both SAR and optical indices, e.g. in (Dostalova et al. 2016).

Grouped k-fold cross-validation was used in the training process, where 10-folds were used, based on *IDs*. *IDs* helped to keep records of the same area in either training or validation datasets. The MAE scoring function was used to evaluate cross-validation.

Regression Analysis using RFR and Auto-sklearn

Regression analysis was used in this study. The main part of the analysis consisted of comparing the performance of an AutoML approach, auto-sklearn, and RFR in estimating optical VIs from SAR and ancillary data for forests.

An AutoML tool can be described as an out-of-the-box supervised machine learning (ML) approach that enables automatic development of ML pipelines. In case of auto-sklearn, it is able to perform all the data and feature pre-processing, as well as the algorithm selection and its hyperparameter tuning for the user. Finding of the best performing algorithms and their hyperparameters, in literature called as Combined Algorithm Selection and Hyperparameter optimization (CASH), is empowered by Bayesian optimization, concretely by the Sequential Model-Based Optimization for General Algorithm Configuration (SMAC) (Hutter, Hoos, and Leyton-Brown 2011) based on random forest models, developed for Auto-WEKA AutoML framework (Thornton et al. 2013). On top of solving the CASH problem, auto-sklearn also uses meta-learning to warm-start the Bayesian optimization process with identifying similarities in the pre-trained datasets (details in (Feurer et al. 2015)), and thus it significantly speeds up the optimization process. Bayesian optimization ensures that the algorithm can learn from the previous steps in the loop and suggest a better setting (pre-processors, algorithms, hyperparameters) in the next step. At the end, it builds an ensemble of ML models considered by Bayesian optimization. The auto-sklearn ML pipeline optimization is figured in Fig. 4. For regression tasks, auto-sklearn

includes 12 regression algorithms, 15 feature preprocessing algorithms and 5 data preprocessing algorithms, all based on the scikit-learn library [scikit-learn]. Altogether, there are 95 hyperparameters which can be evaluated in pipeline optimization, while most of them are conditional hyperparameters (active based when another hyperparameter is active) (Feurer et al. 2015). Each algorithm with the number of their hyperparameters is listed in Appendix I. Auto-sklearn also supports multi-output regression analysis, but it is allowed only for five available regression models (K-nearest neighbor, Decision tree, Extra Trees, Gaussian Process, Random Forest). Therefore, to include as many regressors in the search space as possible, the analysis was performed for each target optical VI separately.

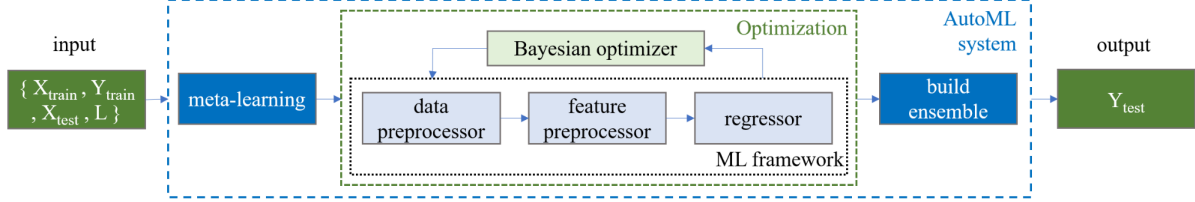


Fig. 4. Auto-sklearn search space pipeline for regression analysis. Based on (Feurer et al. 2015).

The pipeline optimization process is performed until a defined computational budget, which in case of auto-sklearn is time. A longer time usually means a higher chance of finding better-performing pipelines. To test the required optimization length for auto-sklearn, in this study, four different optimization lengths (10 minutes, 1, 6 and 12 hours) were tested. The user can also define how much time can be left for a single model to be performed. In this study, the default value representing one tenth of the overall time limit (the overall computation budget) left for AutoML was used. As a metric to evaluate the final ensemble model (loss function - L), the MAE was used to eliminate the absolute error in the prediction.

A search represents the search of appropriate models, i.e. a combination of feature and data preprocessor, the algorithm with its hyperparameters. One run represents one entire pipeline, i.e. data preprocessor, feature preprocessor, algorithm selection and parameter selection for the algorithm.

Accuracy Assessment and Visual Analysis of the Results

After the successful run, the successful and unsuccessful runs were examined. The best found models were saved together with the description of the models, their weights in the ensemble, duration and cost. Pipelines including all parameters of data and feature pre-processing, model/estimator selection and its hyperparameters were saved as well.

The best found ensemble model was used in inference for the test datasets. The accuracy was evaluated using three metrics: MAE (1) and Root Mean Squared Error (RMSE) (2) and for the comparison of accuracies between different models, the Coefficient of determination, R^2 (3) was used. They are defined as follows:

$$\text{MAE} = \frac{1}{n} \sum_{i=1}^n |y_i - p_i| \quad (1)$$

$$\text{MSE} = \sum_{i=1}^n (y_i - p_i)^2 \quad (2)$$

$$R^2 = \frac{\sum_{i=1}^n (y_i - p_i)^2}{\sum_{i=1}^n (y_i - \bar{y})^2} \quad (3)$$

where y_i stands for the i -th actual (label) value, p_i stands for the predicted/estimated value, \bar{y} is the calculated average of the actual values n is the sample size (the size of the test set).

Because of the stochastic nature of ML algorithms, 3 different runs of RFR and auto-sklearn were performed for accuracy assessment, while the average of accuracy scores of these runs were calculated for each estimated VI and for each length of auto-sklearn optimization runs.

After selecting the best regressor, a time series analysis was performed in selected forest areas (case studies) to compare the original and predicted index time series curves for healthy broad-leaved, coniferous and

disturbed coniferous forests. For these time series, an averaging moving window of size 5 was applied for better visualizations.

Furthermore, a spatial comparison of the original and predicted NDVI was performed for the test area. A map of absolute errors was also produced, while calculating the MAE and the standard deviation for the selected test area. As the forest type is included in the input dataset for training, forest type differentiation (coniferous versus broad-leaved forests) is needed for inference as well. The CLC and CGLCL layers have a 100 m minimal mapping unit; therefore, a more detailed dataset was used for this inference, the Copernicus High Resolution Layers (HRL) from 2018, which is generated in 10 m spatial resolution.

Results

Data Exploration

In the first step, data exploration was performed to assess data availability in the studied period and to understand when they are reliable enough to extract meaningful information and discover unwanted patterns. Furthermore, time series analysis of both healthy and disturbed forests was performed for SAR and optical features to understand the seasonal behavior of forests and similarities using both sensors. Due to the fact that input data are based on the availability of cloud-, shadow- and snow-free pixels of S2 data, data gaps can be observed for various periods in 2021. Generally, there are more measurements available for broad-leaved forests (~15000) compared to both healthy and disturbed conifers (both ~11000). The lack of data in the first 45 days and about the last 30 days of the year with less than 50 and less than 70 measurements, respectively, is apparent from the data distribution in Fig. 5. These periods represent the winter time in Czechia with a usually cloudy and snow-covered landscape, especially in the higher altitude areas, typical for coniferous forests. Less available data (less than 250 measurements) can also be observed for DOYs 140-154 for each forest type, DOYs 126-140 for broad-leaved forests, and DOYs 98-112 for disturbed coniferous forests. Less than 100 measurements were available for DOYs 308-322 for both healthy and disturbed coniferous forests. On the other hand, as expected, most of the data are available during summer (June-September) with the highest number of measurements for each forest type between DOYs 154 and 168 (June 3 - June 17).

Overall, a lack of input data in winter was observed due to cloud or snow cover in the optical images. Although it is a potential issue in ML model training, the inclusion of available winter data was crucial for all-year VI estimation.

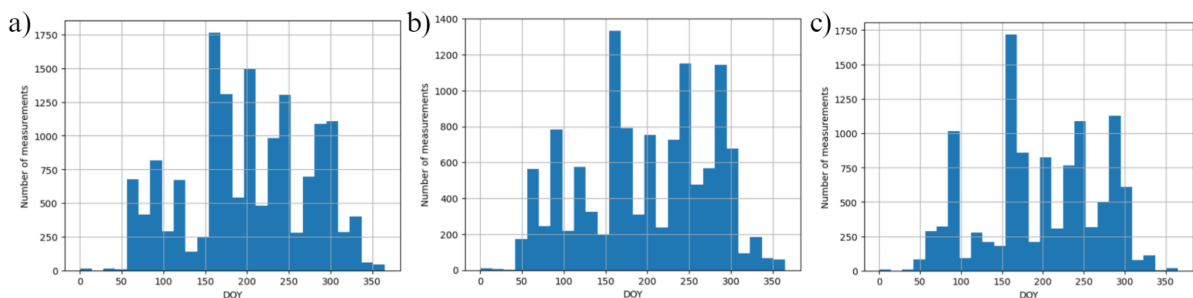


Fig. 5. Data distribution for a) broad-leaved, b) coniferous and c) disturbed coniferous forests based on DOY in 2021. The number of measurements are divided into 14-day intervals.

Time series analysis of an optical VI, the NDVI, showed a clear and expected seasonal pattern for deciduous forests with low values in the beginning of the year, increase in summertime (0.89 on average) and decrease in late spring with lowest values during wintertime (0.54 on average) (Fig. 6a). The NDVI time series for coniferous forests shows a rather stable behavior throughout the year with a slight increase toward winter with a yearly average of 0.78 (Fig. 6c). Some areas represent some noise throughout the year, even in the summertime, which can be caused by not sufficient cloud and shadow masking, even if a combination of three cloud masking approaches was used. This noise is more apparent in coniferous time series because these areas are located in higher elevations (Table II), which are more affected by cloud or haze cover. In the case of disturbed conifers,

where the disturbance could occur any time of the year, the time series shows a noisy appearance with a generally lower magnitude compared to healthy areas. As observed previously, lack of data in the wintertime is also apparent in the time series of disturbed conifers, causing a rather noisy behavior of the signal with high fluctuation.

In case of SAR time series, a seasonal behavior was found in VH polarization for both coniferous and broad-leaved forests. Seasonality in VV backscatter was found for coniferous forests, while the backscatter behavior throughout the year was rather stable for broad-leaved forests. However, the seasonalities found are opposite in nature, i.e. the VH backscatter increases in summertime for coniferous forests, with a mean of -14.3 dB for summer compared to -15.8 dB in winter (Fig. 6b), while it decreases for deciduous forests, while statistically obtaining a mean of -15.1 dB for both winter and summer periods due to high variation in data (Fig. 6d). On average, higher VH and VV values were obtained for broad-leaved forests (-14.9 dB on average) compared to coniferous forests (-15.1 dB) or disturbed conifers (-16.7 dB). Similarly as in the NDVI time series, the SAR time series of disturbed conifers showed a higher fluctuation of backscatter values during the year.

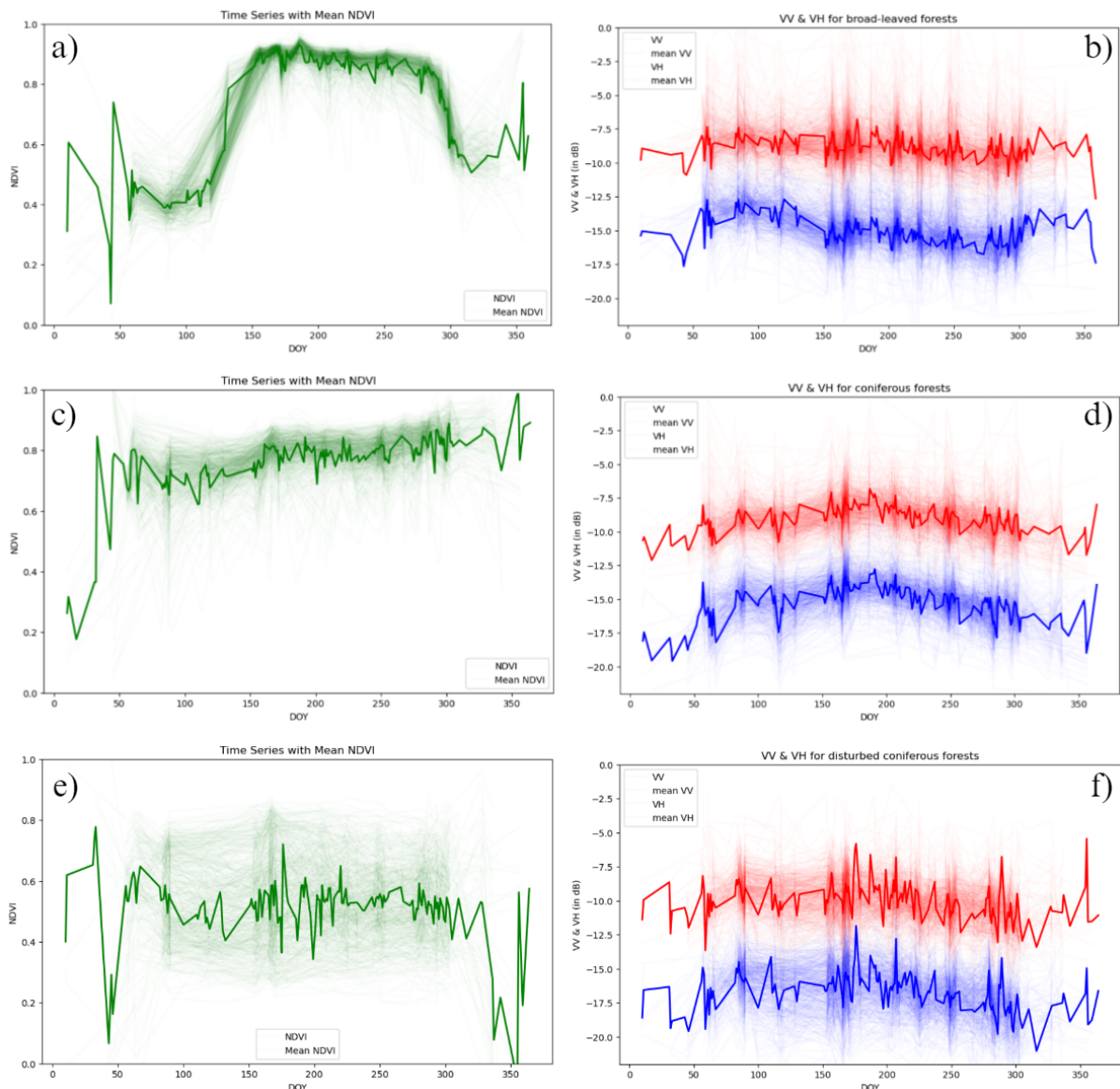


Fig. 6. Average and individual time series of optical (NDVI) and SAR features (VV and VH) using all input data for broad-leaved (a and b), coniferous (c and d) and disturbed coniferous forests (e and f).

Selecting Input Features: Pairwise Correlation Analysis

To avoid redundancy and to find the right combination of input features, a pairwise correlation analysis was performed using all input features. The focus was on finding very highly correlated features, especially SAR features, to exclude them from further analysis. The pairwise correlation analysis (Fig. 7) showed high to perfect negative or positive correlation between some of the SAR features. Pearson's correlation $r = +/-1.00$ was found for each combination between RVI, RFDI and NRPB. They had $r = +/-1.00$ also with VV/VH and VH/VV and had a very high correlation with VH ($\sim +/- 0.86$) and a high correlation with VV polarization ($\sim +/- 0.64$). Therefore, these indices were excluded from further analysis because they do not provide any new information to the ML model. The VV/VH and VH/VV were further examined, as they had a mutual correlation of 100%. As the VV/VH correlation was lower with the VV and VH polarizations, it was kept in the input feature set. The DPSVI index modifications (DPSVI_o, DPSVI_m and DPSVI_n) had slightly different correlations with other input features, while the DPSVI_o and DPSVI_n had a mutual correlation of 0.82. Thus, the correlation of these indices was further investigated with other features. Based on the fact that DPSVI_n had a similar correlation with DPSVI_m with several features (the same for temperature, only 0.01 difference with VV), DPSVI_n was excluded from further analysis. As expected, a high correlation (~ 0.50) was found between the LIA and SAR indices. This is caused by the fact that the input datasets included data derived from every possible acquisition geometry, i. e. both from ascending and descending orbits with different incidence angles in the case of overlying paths. Although a very high correlation was also found between the VV and VH polarization (0.86), they were included in the final selection of input features to preserve the original and only two polarizations of the S1 data. Despite the high correlation of temperature with the time feature (DOY_{cos}), it was kept in the input feature set due to its strong correlation with C-band SAR backscatter found in (Olesk et al. 2015), and due to the fact that freezing conditions and temperatures below 1 °C were found to cause a significant decrease in SAR backscatter over forests, e.g. in (Rüetschi, Small, and Waser 2019; Benninga, van der Velde, and Su 2019; Ranson and Sun 2000).

The preserved features used in the next analysis were: VV, VH, incidence angle (angle), VV/VH, DPSVI_o, DPSVI_m as SAR features; angle, LIA, and DEM (elevation) as DEM features; sum of precipitation 12 hours prior to SAR acquisition (prec._{12h}) and temperature at the time of SAR acquisition (temp.) as weather features; the forest type as a differentiating feature between coniferous and broad-leaved forests; and DOY_{sin} and DOY_{cos} containing information about the time of the corresponding SAR acquisition.

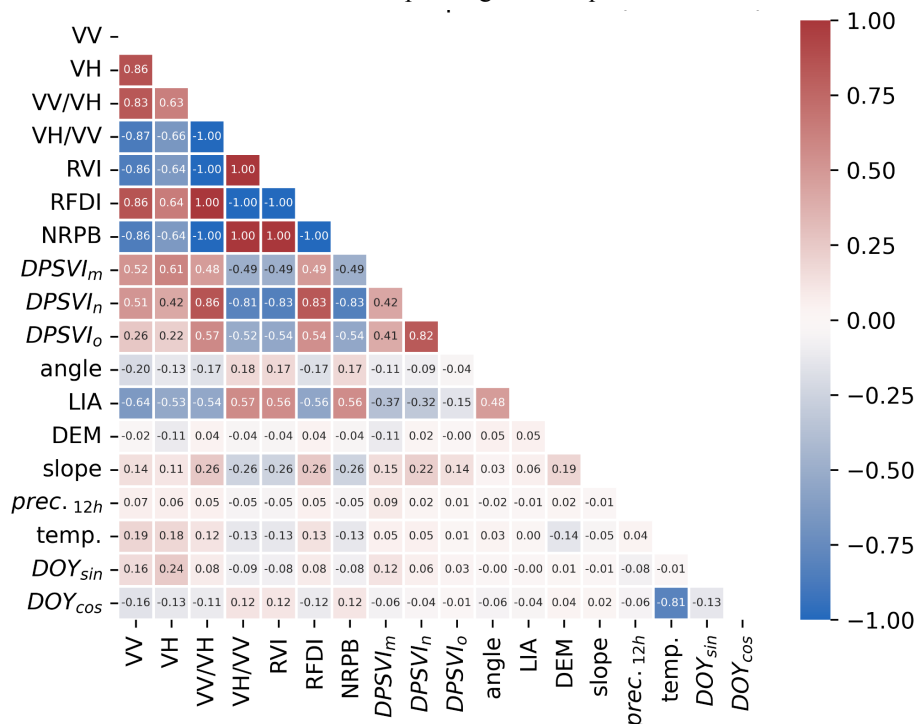


Fig. 7. Pairwise correlation between all input features for all data points (n=37818).

Improving Robustness with Inclusion of Disturbed Forest Areas

A comparison of model performances (statistically and visually in time series analysis) and feature importances when only healthy forests and also disturbed forests are used in the training is presented here. When using only healthy forest areas as input dataset (for training, validation and testing) for the model, the RFR was able to predict NDVI with R^2 of 86%, MAE of 0.035 and with a very good match of estimated NDVI time series and original NDVI from S2 (Fig. 8a and b). However, in this case, the time features (DOY_{sin} and DOY_{cos}) represented more than 58% importance and the forest-type had about 28%. Other features had only a marginal effect on the results (<3%), while all SAR features had less than 1% (Fig. 9a). This means it would be enough to have only time and forest type information to estimate time series of the NDVI for healthy forests. On the other hand, estimation of NDVI for disturbed forests (Fig. 8c and d) shows almost identical behavior to estimation of healthy coniferous forest due to the fact that these disturbed areas represented coniferous forests and had assigned coniferous type in the inference.

When a higher variance was included in the input dataset, i.e. when time series data of 600 disturbed forest areas were added, the R^2 decreased to 68% and MAE increased to 0.072. Although the statistical results became worse, the visual comparison of original and estimated time series shows still a very good match for healthy forest areas (Fig. 8 a and b). Furthermore, the estimation for disturbed forests shows a good match with the original NDVI with a detectable change (disturbance event) in the time series with a decrease in the estimated NDVI at DOY range of 200-206 Fig. 8c and d). Significantly lower values are observed for the previously disturbed area compared to a healthy coniferous area while also following the original NDVI time series curve (Fig. 8 d). Feature importance (Fig. 9b) shows that the forest type is the most important feature with 23%, while VH has the second largest importance with 15%, followed by time features (15% and 11%), elevation (8%) and temperature (6%).

To improve the robustness of the estimates, it is also necessary to include disturbed forest areas in training.

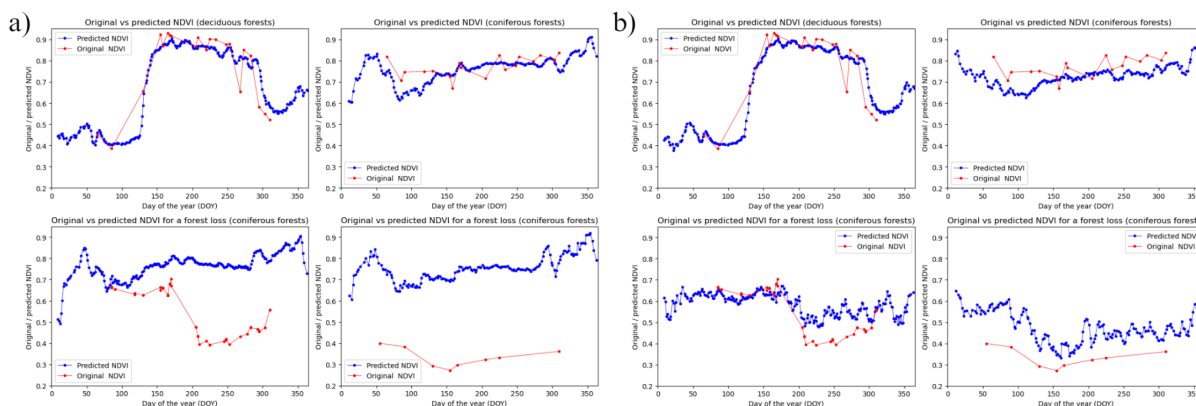


Fig. 8. Time series for optical NDVI and predicted NDVI when using only healthy forests in the training in a) and predictions when using both healthy and disturbed forests in the training b).

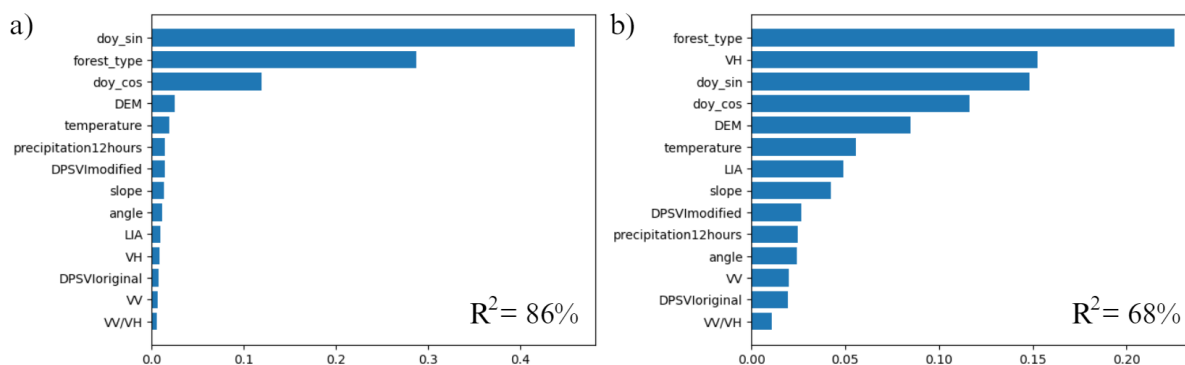


Fig. 9. Feature importance when using only healthy forests (a) or using healthy and disturbed forests (b).

The Effect of Different Ancillary Data on Regression Results

The comparison of RFR and Auto-sklearn (run for 1 hour) with different input feature sets containing only SAR data, SAR data with information generated from DEM and using all input features (SAR with DEM and weather information) is presented in Table VI. This comparison showed that using all input features reveals the best results in all accuracy metrics and for each VI. It should be noted that forest type and time information (DOY_{sin} and DOY_{cos}) were included in each feature combination. The use of features derived from the DEM (elevation, slope and LIA) with SAR data, represented a 3% increase in R^2 on average for RFR compared to pure SAR data. Using additional weather information (precipitation 12 hours prior to the acquisition and temperature at the time of the acquisition), an additional improvement was made, specifically 1% in R^2 on average. In the case of Auto-sklearn, these improvements were smaller in magnitude, but it was still possible to observe a gradual increase of R^2 when adding DEM features and additional weather features (by 1.5% and 0.9%, respectively). Generally, better results were obtained by auto-sklearn compared to RFR, except for FAPAR estimation, where the best results were obtained by RFR (better by 0.5%). The greatest improvement using Auto-sklearn compared to RFR was achieved for NDVI (1.4%).

Table VI. Evaluation of results using input data with only SAR features, SAR and DEM, and using all available features with RFR and auto-sklearn (AS) regression with an optimization run for 1 hour averaged across 3 repetitions. The best results are highlighted in bold.

	RFR SAR only			RFR SAR + DEM			RFR ALL		
	MAE	MSE	R^2 (%)	MAE	MSE	R^2 (%)	MAE	MSE	R^2 (%)
LAI	.349	.223	80.42	.329	.202	82.22	.320	.192	83.13
FAPAR	.084	.014	72.62	.079	.012	75.82	.077	.011	77.34
EVI	.057	.006	80.25	.054	.006	83.02	.053	.006	83.17
NDVI	.079	.013	63.14	.075	.012	66.00	.072	.011	67.85

	AS SAR			AS SAR + DEM			AS ALL		
	MAE	MSE	R^2 (%)	MAE	MSE	R^2 (%)	MAE	MSE	R^2 (%)
LAI	.332	.204	82.10	.322	.191	83.21	.318	.189	83.41
FAPAR	.080	.012	75.21	.079	.012	76.51	.078	.011	76.74
EVI	.054	.006	82.68	.053	.005	83.47	.052	.005	83.73
NDVI	.075	.012	66.00	.073	.011	68.12	.071	.011	69.23

Evaluation of Auto-sklearn and the Best Performing Models

In this step, the performance of Auto-sklearn was assessed for different training lengths, while the most efficient models were selected for further analysis. Additionally, an analysis of accuracy and errors over time was also performed for each estimated VI. With the increasing time budget for auto-sklearn optimization length, an increase of tested pipelines and also an increase of share of successfully finished pipelines on all evaluated runs can be detected (Fig. 10). This is an expected behavior of the AutoML approaches. In the case of 10-minute runs, on average, 98 pipelines were tested, while only 41% of these pipelines were finished successfully. In the 1 hour run, on average 151 pipelines were tested and 55% were successful. In 6 hour runs, 65% of the pipelines ended successfully from the total of 250 evaluated pipelines. The number of evaluated pipelines almost doubled for 12 hour runs, with on average 366 tested pipelines and a 70% success rate, that is, on average 258 pipelines were successfully finished.

In the case of accuracy assessment, a noticeable improvement can be found mainly when increasing the optimization length from 10 to 60 minutes. The greatest improvement was made to NDVI and FAPAR, with

4.2% and 2.3% of improvement in R^2 , respectively. Although statistically the best results were achieved for 12 hour runs, improvements from 1 to 6 hours and further to 12 hours of run length were only marginal (in both cases $<0.25\%$ in R^2). On average, low overall errors were achieved for each VI, 0.32 of MAE for LAI and 0.05-0.09 of MAE for other indices, and 0.19 of MSE for LAI and 0.005-0.016 for other indices. In case of the coefficient of determination, the highest R^2 was achieved for EVI with 83.73% followed by LAI with 83.41%. The lowest R^2 was achieved by NDVI with 69.23%.

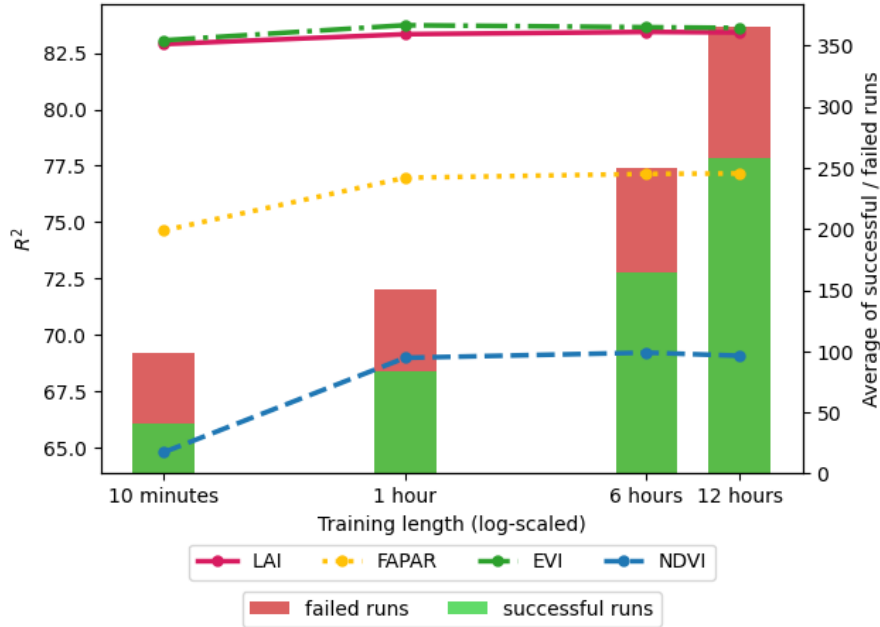


Fig. 10. Evaluation of results using input data using all available features with auto-sklearn regression for different lengths of optimization runs, each averaged across 3 repetitions.

Besides the increase in accuracy (and decrease in error metrics), the optimization length was also considered when selecting the most efficient optimization length of auto-sklearn. Based on these considerations, Auto-sklearn models with 1 hour optimization length were selected as the most efficient one. For further analysis and generating the next results and outputs, only one single model can be used; therefore, the best performing models (out of three tested for each VI) were selected (Table VII). These models are represented by ensemble models of several algorithms, almost entirely composed of Gradient Boosting algorithms (GB), as can be seen in Table VII. The maximum size of the final ensemble was 7 for LAI with 7 GB with single-model weights ranging from 2% to 48%.

Table VII. Composition of performing Auto-sklearn models using 1 hour optimization runs.

	LAI	FAPAR	EVI	NDVI
Composition of models	7xGB	4xGB	6xGB	5xGB

Analysis of accuracy and error over time (Fig. 11) revealed a general agreement with data availability, i.e., the highest errors were found in wintertime, when no sufficient number of observations was available (Fig. 5). On the other hand, the lowest errors and highest R^2 values were found in periods where a sufficient number of measurements were available. A deviation from these results was found in the case of LAI, where high errors occurred during the summer period. Some of the R^2 values were masked in wintertime, as they did not contain enough measurements (< 2) or gave errors, meaning that no correlation was found between the observed and estimated values. The highest R^2 values were achieved between DOYs 140 (20 May) and 308 (4 November), 83% for LAI and 75% for NDVI. A decrease in R^2 can be observed between DOYs 126-140 (around 40%) due to the data unavailability in this period (Figure 5). Relatively high R^2 values ($>50\%$) were achieved for some periods at the end of the year for LAI, when a moderate number of observations were available.

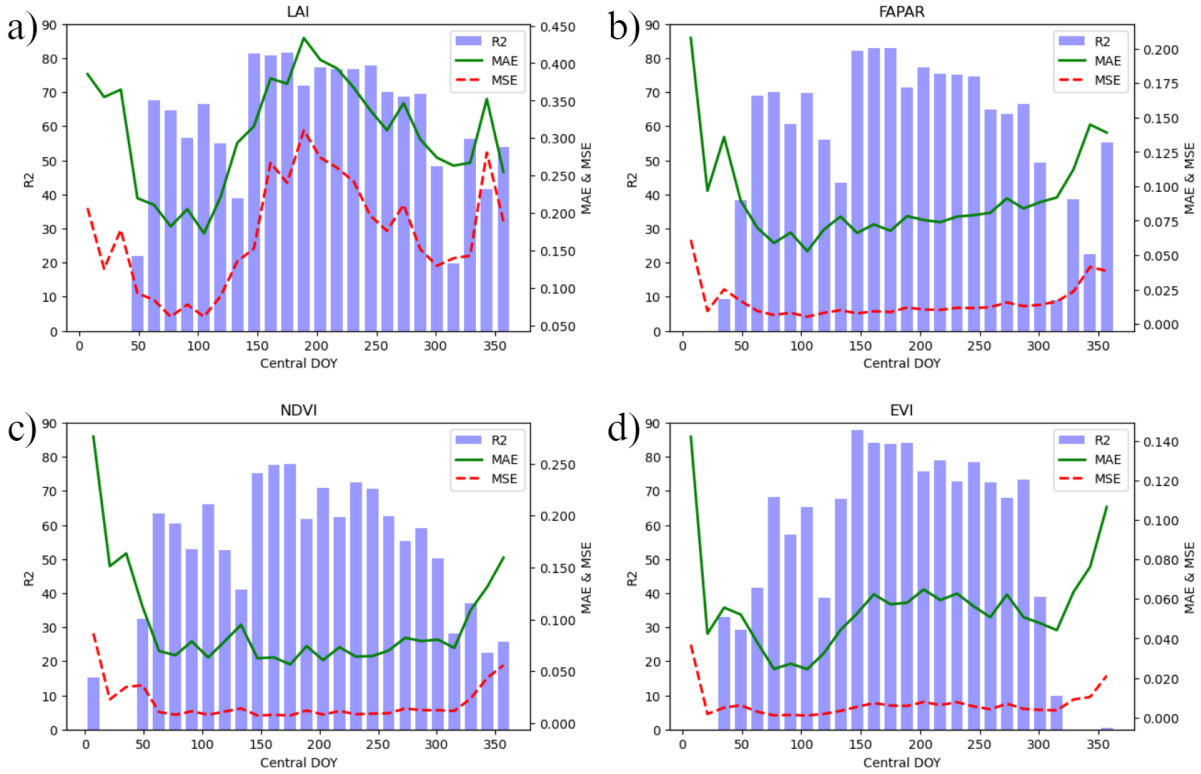


Fig. 11. Time series of accuracies (R^2) and errors over time for LAI (a), FAPAR (b), NDVI (c) and EVI (d) based on test sets using the best performing Auto-sklearn models for 14-day time steps.

Time Series and Spatial Analysis of the Results

To test the robustness of the models, a time series analysis was performed for selected case studies from Table II comparing original VI time series and SAR-based time series. Furthermore, inference for the entire test area from Table III was performed to analyze the spatial behavior of the results. The time series analysis for selected case studies (Fig. 12) shows generally a good agreement between the original S2 and the estimated time series for each selected forest type (broad-leaved, coniferous, disturbed coniferous during 2021 and disturbed coniferous forest before 2021) and shows a generally good differentiation between forest types with the ability to estimate the time of the disturbance event. For the selected case studies, 9-21 measurements were available from the S2 mission, while from the S1 SAR mission, it was 175-236 depending on the overlap in acquisition paths over the selected area. The SAR data time series covered the whole year.

Similarly to the S2 time series of the selected indices, the differentiation between broad-leaved (Fig. 12 green curves) and coniferous forests (Fig. 12 blue curves) is straightforward using the estimated SAR-based VI. This is due to the low values of the indices during the leaf-off period and a high value for the leaf-on period for broad-leaved forests and the generally stable behavior of coniferous forests throughout the year. The lowest values for each original and estimated VIs were achieved for the former coniferous forest area where a disturbance event occurred before 2021 (Fig. 12 red curves). An overestimation of SAR-based VIs can be detected for this case study, especially during winter. The drop in the original optical VI time series for case study 3 is detectable between DOYs 170 (June 19) and 205 (July 25) (Fig. 12 dashed orange curve). On the other hand, in the SAR-based VI estimation (Fig. 12 orange curve), the drop is detectable around DOY 203 (22 July 2021) between DOYs 200-206, with an increase in time series curve fluctuation after the disturbance event. The fluctuation of the estimated time series for both disturbed areas is generally high even if the average moving window of size 5 was used in Fig. 12. Furthermore, compared to the healthy coniferous case study, lower VI values can be found in the pre-disturbance state in case study 3, suggesting that the condition of the forest was not in perfect shape before the disturbance.

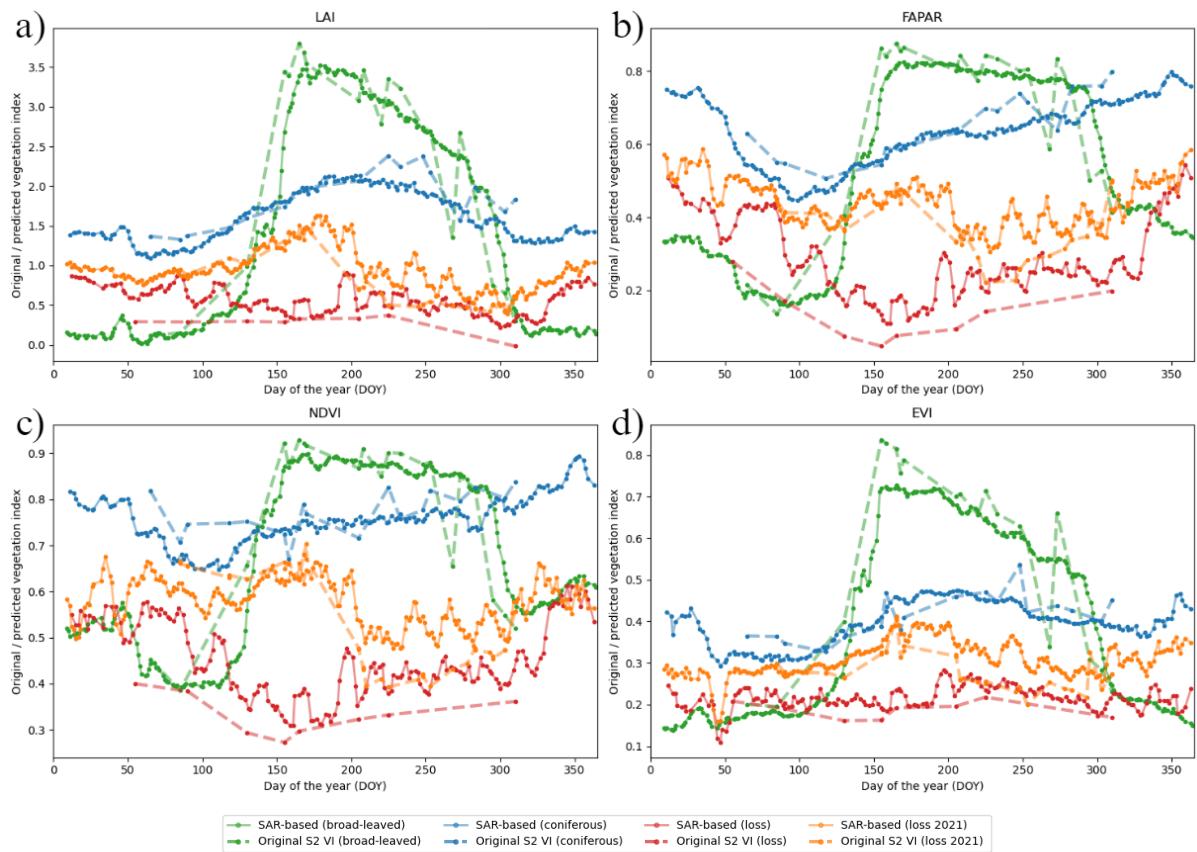


Fig. 12. Time series of original and estimated VIs for LAI (a), FAPAR (b), NDVI (c) and EVI (d).

In the spatial analysis of the estimated SAR-based NDVI, one can easily differentiate between coniferous and broad-leaved forest areas due to their difference in magnitude of the NDVI (higher NDVI for broad-leaved forests). Disturbed or non-forest areas are represented by low NDVI values both in the original S2-based and SAR-based NDVI estimation. The spatial analysis also shows great agreement of SAR-based VIs with the original optical-based VIs with a MAE of 0.047 with a standard deviation of 0.050 (Fig. 13). The highest errors were found in areas where recent forest disturbance occurred (mainly fresh clear-cuts in 2021), which were not captured by the HRL dataset from 2018, that is in the central and south-east part of the study area. Higher errors can be found on the borders of between forested and non-forested areas and on the borders of coniferous and deciduous forests.

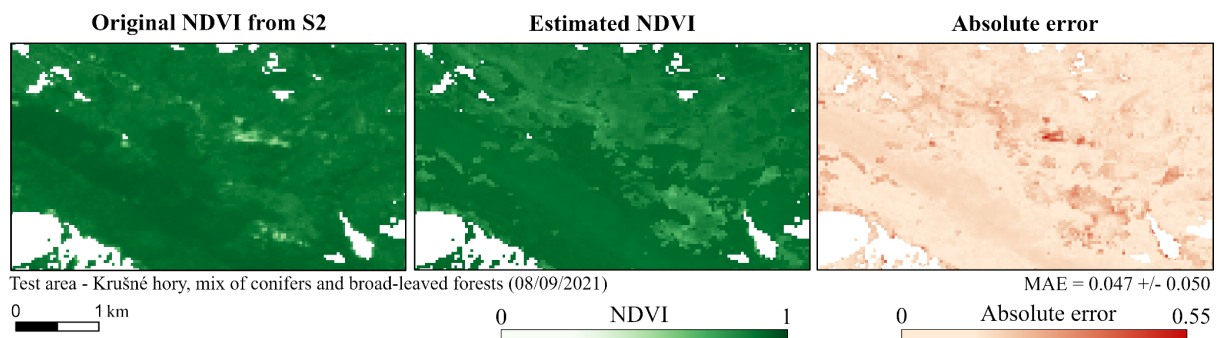


Fig. 13. Comparison of original NDVI (a), predicted NDVI (b) and absolute errors (c) for the entire Krušné hory test area.

Discussion

In this study, SAR and ancillary data were tested with the use of machine learning techniques to estimate time series of four optical VIs for forest monitoring. For this purpose, in the first step, a multi-modal and multi-temporal dataset for 2021 over Czechia was created in GEE (MMT-GEE). The basis of the MMT-GEE dataset is made up of spatially and temporally aligned preprocessed S1 and S2 data (based on a 24-hour difference). The S2 data cloud-masking uses three different approaches to ensure the exclusion of as many pixels affected by cloud, shadow and snow cover as possible. Furthermore, this dataset includes temporally aligned weather information (aligned with S1 acquisitions) derived from the ERA-5 Land dataset with a half-hourly temporal resolution (precipitation and temperature) and information derived from COP-DEM (elevation, slope, LIA). Access and processing of hundreds of S1 and S2 images and thousands of ERA-5 Land images without the need for any local computational power or storage was possible using the GEE cloud-based platform. The MMT-GEE dataset is unique because it enables an easy further extension with other ancillary datasets, customization of the satellite data preprocessing pipeline and feature extraction, and can be generated for any time period (based on data availability) and over any geographical region, both locally and globally. Therefore, this dataset addresses various challenges of the currently used satellite-based datasets, as presented in (Schmitt et al. 2023). Therefore, the GEE code for generating the multi-modal and multi-temporal MMT-GEE dataset is available in the GitHub repository of this work at github.com/palubad/SAR-based-VIs-AutoML [*not accessible during the review process*]. In the present form, the MMT-GEE is prepared for export of tabular data, but the next work will be focus on improving the MMT-GEE to export image patches for deep learning analyzes to fully address the requirements for deep learning analyzes in (Schmitt et al. 2023) as well.

The MMT-GEE dataset was then used to create the input data for further analysis. First, forest areas were automatically generated using forest masks for healthy coniferous and broad-leaved forests, as well as for disturbed coniferous forests based on spatial overlap of four different forest and land cover datasets. Although this combination of datasets was used to minimize the possible errors in forest delineation in each of the datasets, it was not sufficient to achieve 100% accuracy. Therefore, automatically generated forest areas were manually verified using high-resolution GEP satellite imagery from the winter and summer seasons, and only areas that actually represented healthy or disturbed forest areas were included in the analysis. The validation process was important to include only valid data in the further analysis, which resulted in the selected 1800 forest areas representing 40x40m areas.

Data preprocessing and preparation was followed by data exploration, where the basic assumption that the SAR backscatter time series has seasonal variation for forests was confirmed in this study (Fig. 6 and 12), similarly as in previous studies (Dostalova et al. 2016; Frison et al. 2018). Seasonal variations were found for both examined forest types, while their seasonality was opposite, with a backscatter increase in summer for conifers and a decrease for broad-leaved forests. Coniferous forests experienced the highest VH backscatter in summertime and the lowest for wintertime, similarly to in (Dostalova et al. 2016). The seasonal variation in broad-leaved forests with higher values during leaf-off periods can be attributed to a decrease in attenuation by the tree crown, especially leaves with sizes similar or larger than the C-band wavelength (~5 cm), and therefore a higher received backscatter from multiple scattering between the primary and secondary branches, or even the tree trunk and soil depending on the tree crown density. Seasonality in conifers for SAR backscatter, in contrast to the almost stable behavior in optical indices, is often attributed to the needle loss during colder conditions and effects of understory vegetation, which can be formed by deciduous vegetation types (Dostalova et al. 2016; Dostálová et al. 2018; 2021). Lower backscatter values can also be attributed to a lower moisture content in vegetation (mainly needles) during hot and dry summer days, causing greater penetration of the signal into the tree crown and less backscatter returned to the SAR sensor. Generally, higher backscatter values were obtained for VV for both types of forest, which confirms previous findings (Dostalova et al. 2016; Dostálová et al. 2018; Paluba et al. 2021). A clearer and more distinct seasonality was found in the VH polarization for both forest types compared to VV due to the fact that the VH polarization is more strongly affected by volume scattering (Richards 2009; Vreugdenhil et al. 2018).

Selection of the best performing input feature set is important in any ML pipeline; therefore, the similarities in input features were tested using pairwise correlation in the first step. It showed that most of the derived SAR

polarimetric indices had almost identical behavior ($r > |0.86|$) with other SAR indices and VV and VH polarizations; therefore five (RVI, RFDI, VH/VV, NRPB and $DPSVI_n$) out of eight suggested polarimetric indices were excluded from further analysis. The high correlation between different SAR polarimetric indices suggests that they did not provide new information to the algorithms. Only the VV/VH, $DPSVI_o$, and $DPSVI_m$ polarimetric indices, together with VV and VH polarizations, were used as SAR features. In addition to the forest type feature, the VH polarization showed the highest importance for the RFR model, most likely due to the high correlation of VH with vegetation density and VIs, as also found in previous studies (Alvarez-Mozos et al. 2021; Filgueiras et al. 2019; Holtgrave et al. 2020; Jiao, McNairn, and Dingle Robertson 2021; Moran et al. 2012).

Further analysis of input feature combinations showed that including DEM-based features to the SAR-based ones improves the R^2 by 3% on average and inclusion of both DEM- and weather-based data improved the R^2 by another 1% on average. Radiometric terrain correction was not used in this work; therefore, the per-pixel LIA feature holds important information about the differences between ascending and descending orbits and acquisition paths in mountainous areas, such as low LIAs for slopes facing the SAR sensor and high LIAs for slopes facing away. Improvement in the accuracy of NDVI estimation from SAR data using LIA was also found in (Filgueiras et al. 2019). Moreover, elevation and slope information can provide information about differences in forests (height, density, tree crown structure) that are specific for different altitudes and slopes. The presented results are similar to those in Roßberg and Schmitt (2022), where models using more input data (SAR, DEM and land cover) achieved better results. The influence of weather information on the results can be attributed to the findings that precipitation (which therefore increases soil moisture) can affect the backscatter from forests in (Benninga, van der Velde, and Su 2019). Therefore, the influence of precipitation could have been identified and eliminated when using SAR and precipitation data as input features. A correlation was also found between SAR backscatter and temperatures (Rüetschi, Small, and Waser 2019; Olesk et al. 2015), while temperatures below 1°C were found to negatively affect SAR backscatter in (Benninga, van der Velde, and Su 2019; Ranson and Sun 2000). Moreover, the tested optical VIs have a clear correlation with temperature, i.e. low values in wintertime and high values in summer. However, further studies are needed to investigate the impact of environmental effects on SAR backscatter.

Monitoring forest changes using RS data and methods is crucial for tracking current greenhouse gas emissions, biodiversity indicators, or illegal logging activities and their consequences. Especially, on a regional scale it can help to provide a rapid adequate response in forest management in case of sudden changes. Therefore, an emphasis was placed on a successful estimation of VIs for both healthy and disturbed areas in this study. For this purpose, it was important to select an appropriate input dataset that contains time series of both healthy and disturbed forest areas. In this study, the importance of increasing variation in input dataset was examined by comparing the results of the models using only healthy input data and a dataset where disturbed areas were included. As expected, when using only healthy datasets, the inference on healthy case studies worked well with very high accuracy, while the estimations on disturbed case studies showed a time series corresponding to a healthy forest area, i.e. that model was not able to detect the forest change. Furthermore, the RFR feature importance (permutation analysis) revealed that in these cases, the SAR and other satellite-based features had a negligible impact on the final results, while the information about time and forest type had crucial effects (Fig. 9). This means that only information on time and forest type would be sufficient to estimate the NDVI time series for healthy forests. On the other hand, when disturbed data were included, time series estimations for disturbed case studies showed expected results for both healthy and disturbed forest areas where the VH polarization was the second most important feature after forest type.

The proposed methodology effectively differentiated between healthy and disturbed forest areas. In addition, the detection of changes using SAR-based VIs, especially for LAI, FAPAR and NDVI, were significantly more rapid than for the original S2 data. They were able to achieve a sub-weekly accuracy in detecting changes, whereas the original S2 data exhibited over a month of uncertainty between the last time step of a healthy state of the forest and the first one in a disturbed state. This uncertainty depends on the availability of cloud-free S2 measurements over the study area, while, on the other hand, all possible S1 acquisitions can be used to generate a SAR-based VI. The number of S1 acquisitions in 2021 was greater than 230 in two case studies and around 175 in the other two, while the number of cloud-free S2 measurements for the same areas ranged from 9 to 21. This brings great advantages when monitoring forest changes in applications where near real-time information is

required, but also in cases where the exact date of change needs to be determined retrospectively. However, it should be noted that this study was carried out for 2021, where both S1-A and S1-B were operational; therefore this high temporal resolution is scheduled to be restored in the first quarter of 2024 (ESA 2023).

Machine learning techniques are nowadays more and more used tools in RS in general, but also for similar tasks including estimating optical vegetation indices from SAR data, including traditional ML, e.g. in (Filgueiras et al. 2019) or (dos Santos et al. 2022), and DL approaches, e.g. in (Roßberg and Schmitt 2022) and (Roßberg and Schmitt 2023). The RFR was found to be a well-performing ML algorithm in previous studies (in (Filgueiras et al. 2019) and (dos Santos et al. 2022)), therefore it was selected for this study as well. AutoML methods save the researcher's time by automating repetitive and time-consuming tasks, efficiently exploring the algorithm and hyperparameter space. It can also improve performance, as it uses ensembles to combine the best found models. Given these facts, AutoML makes ML accessible to users with less ML experience and allows them to develop competitive models. On the other hand, it has its limitations, e.g., it may not capture domain-specific knowledge as effectively as manual selection of algorithms. It has limited transparency and interpretability in model selection and hyperparameter optimization. There is also a lack of customization because it has a limited support for highly specialized or novel techniques. Moreover, most of the AutoML libraries are prepared for tabular data, but some are for image data, such as Auto-Keras (Jin et al. 2023).

When comparing AutoML with the traditional RFR, AutoML with just a 1-hour run slightly outperformed RFR in all, but one case (FAPAR), where Auto-sklearn achieved lower R^2 by 0.5%. Even if Auto-sklearn achieved better results, it is important to consider the time and computational resources needed to achieve better results with an appropriate number of successful runs. Using RFR with its default settings, the results can be obtained in seconds. Moreover, further improvements using Auto-sklearn with a longer optimization run length (6 or 12 hours) were negligible ($<0.25\%$) compared to an improvement of 10 to 60 minutes; therefore, only models with 1 hour runs were used in the analyzes of this study. The most frequent algorithm included in the best resulting ensemble models was the Gradient Boosting, as the state-of-the-art algorithm between the traditional ML algorithms.

The analysis of accuracy and errors over time showed lower accuracy in wintertime, which is caused by the data unavailability in this period. Due to S2 data masking, in some periods of the year, only a few S2 measurements were available for analysis. Moreover, even if a combination of three cloud, shadow and snow masking algorithms were used, some defected pixels could still be present in the dataset, causing errors in input dataset, especially in wintertime. In (dos Santos, Da Silva, and do Amaral 2021) and (dos Santos et al. 2022), a better accuracy was found in the dry season compared to the rainy season, which can also be attributed to the lower availability of S2-S1 data combinations.

A generally higher fluctuation of estimated VIs for disturbed areas compared to healthy forests can be caused by several factors, e.g. higher heterogeneity and higher soil roughness of clear-cut areas with possible left-overs after the clear-cut and disturbed soil after the use of heavy machinery; no attenuation of SAR signal by tree crowns and therefore high contribution of soil with greater influence of environmental factors (e.g. precipitation and increased soil moisture, snow cover or frozen conditions). Lower values of case study 3 during the pre-disturbance state indicate a not perfect condition of forests, suggesting that using both the original S2 and the estimated SAR-based VI it is possible to monitor the health status of forests. This finding can serve as an important basis for studying forest health or forest degradation, such as the stages of bark beetle infestation, using SAR time series.

Errors in spatial analysis usually had two main sources: the inaccuracy of forest type databases and in areas of current forest changes. As found in the permutation analysis (feature importance), forest type is a leading feature due to which it is possible to differentiate between the seasonality of coniferous and broad-leaved forests. Furthermore, the areas of broad-leaved forest loss were not included in the training process, so it is not possible to detect broad-leaved forest loss using SAR-based VIs. Therefore, the accuracy of the forest type database in a required spatial resolution is a fundamental element in estimating the VIs time series and spatially (for a broader area) for a single acquisition. Errors due to recent forest changes are related to the fact that a disturbed or cleared forest can have a very high variance in SAR backscatter due to structural changes and various environmental effects, as discussed above.

Further improvements are needed to reduce errors in periods with a lack of data. This can be solved in the next studies by expanding the time range of the data, such as adding data from more years, not only from 2021.

As this study served as a case study for the temperate forests of Czechia, it will be important to apply and test the proposed methodology in other geographic and climatic conditions or globally. The noisy behavior of estimated SAR-based VIs for disturbed areas needs to be improved to achieve more timely estimations of disturbance events. Adding more disturbed forest areas to train the models would benefit from this task. This study was carried out for S1 data for 2021 when both the S1-A and S1-B satellites were operating, to use the highest possible temporal resolution. However, the loss of the S1-B satellite at the end of 2021 decreased the temporal resolution for previous years. With the launch of the S1-C satellite, scheduled for March 2024 (ESA 2023), the temporal resolution prior to 2022 will be restored. Moreover, new opportunities will be open for VI estimation using SAR data when freely available L- and P-band data will be available from the NISAR, Rose-L and Biomass missions. Multi-band SAR data fusion could benefit forest monitoring due to the different behavior of L- and C-band signals for various forest types and also for forest degradation. Implementing SAR coherence or using SAR polarimetry with quad-polarizations of the new or existing SAR missions to expand the feature space would also be beneficial to achieve better and more stable results. The use of AutoML is an effective but time and resource consuming process of searching for the best pipelines. Therefore, recent studies are focusing on developing so-called “Green AutoML” approaches (Tornede et al. 2023) allowing one to consider the carbon footprint of the hyperparameter optimization process or proposing methods that are competitive in performance with robust AutoML frameworks, but require only a few seconds to find the best model due to improved meta-learning, for instance TabPFN (Hollmann et al. 2023).

In general, the proposed methodology proved to be appropriate for estimating standard optical VIs with high accuracy. Compared to optical VIs, which are prone to atmospheric effects, the SAR-based VI estimations can provide all-year coverage with up to 237 measurements / year using two Sentinel-1 satellites. SAR-based VIs can serve as an alternative source of information on forest seasonality and dynamics and can benefit from the timely monitoring of forest health status and changes. Moreover, in comparison to global or regional VI products, providing a good temporal resolution (such as 10 days in CGLMS LAI and FAPAR), and better spatial resolution (20 m in a 10 m grid) can be achieved using a SAR-based VI. Moreover, data preprocessing pipelines in GEE (including the MMT-GEE dataset generation), Python Jupyter Notebooks for RFR and AutoML analyses, the best found Auto-sklearn models, and all input datasets are available on GitHub to fully reproduce the results for other researchers.

Conclusion

This study successfully demonstrated the feasibility of employing SAR data and ML techniques to estimate well-known and widely used optical VIs for forest monitoring. SAR data proved to be a reliable proxy for the estimation of the cloud-independent vegetation index, with careful methodological considerations. The study introduced the MMT-GEE dataset, combining spatially and temporally aligned multi-modal and multi-temporal data from S1 and S2, extended with DEM, land cover and weather data in GEE. Integrating ancillary data with SAR data improved the accuracy of VI estimation for each of the VIs tested, with the forest type feature and the VH polarization showing the highest feature importance. However, several tested SAR polarimetric indices were excluded from the analysis (VH/VV, RVI, RFDI, NRPB and DPSVIm) due to their high correlation (100%) between each other and with other SAR features, providing no additional information to ML models. When it comes to tested ML methods, the AutoML framework, auto-sklearn, outperformed RFR for three out of four VIs. One hour of optimization length was found to be sufficient for AutoML to find the most efficient models with appropriate accuracy (R2 of 69-84%) with low errors (0.05-0.32 of MAE), depending on the VI. The best AutoML models comprised mostly GB algorithms with different hyperparameters. The errors in the estimates were mainly due to data unavailability, especially in winter when clouds are highly likely to affect S2 acquisition. In summary, the proposed methodology allows to estimate optical VIs with a better temporal and spatial resolution compared to currently available regional and global databases. The SAR-based VIs are offering a 20 m spatial resolution and a temporal resolution of up to 240 measurements / year when both Sentinel-1 are operational. The proposed methodology also allows monitoring of forest changes, such as logging, on a sub-weekly basis. The GEE code for the MMT-GEE dataset generation and regression analysis codes are made freely available to the research community.

Acknowledgments

This work was supported by the Charles University Grant Agency – Grantová Agentura Univerzity Karlovy (GAUK) Grant No. 412722 and the European Union’s Caroline Herschel Framework Partnership Agreement on Copernicus User Uptake under grant agreement No. FPA 275/G/GRO/COPE/17/10042, project FPCUP (Framework Partnership Agreement on Copernicus User Uptake). The authors would like to thank the Spatial Data Analyst project (NPO_UK_MSMT-16602/2022) funded by the European Union – NextGenerationEU, for providing computational resources needed for AutoML. Daniel Paluba would like to thank the Erasmus+ programme for the financial support during his research stay at the Φ -lab, European Space Agency (ESA) in Frascati, Italy.

Disclosure statement

No potential conflict of interest was reported by the author(s).

Data Availability Statement

Open-access data in the Google Earth Engine platform were used in this study. The *Copernicus High Resolution Layer Forest Type* layers were accessed from land.copernicus.eu/en/products/high-resolution-layer-forest-type. Data preprocessing pipelines in GEE (including the code to generate the multi-modal and multi-temporal dataset MMT-GEE dataset), Python Jupyter Notebooks for RFR and AutoML analyses, the best found Auto-sklearn models, and all input datasets (described in sections *Training and testing data validation*, *Case studies for healthy and disturbed forest time series analysis* and *Test area for spatial comparison of results*) are available on GitHub, at github.com/palubad/SAR-based-VIs-AutoML, to fully reproduce the results for other researchers. **[During the review process, the Github repository is closed. Materials are only available to reviewers under the link provided during the submission.]**

References

- Alvarez-Mozos, J., J. Villanueva, M. Arias, and M. Gonzalez-Audicana. 2021. “Correlation Between NDVI and Sentinel-1 Derived Features for Maize.” In *2021 IEEE International Geoscience and Remote Sensing Symposium IGARSS*, 6773–76. <https://doi.org/10.1109/IGARSS47720.2021.9554099>.
- Ban, Yifang, Puzhao Zhang, Andrea Nascetti, Alexandre R. Bevington, and Michael A. Wulder. 2020. “Near Real-Time Wildfire Progression Monitoring with Sentinel-1 SAR Time Series and Deep Learning.” *Scientific Reports* 10 (1): 1322. <https://doi.org/10.1038/s41598-019-56967-x>.
- Bartels, Samuel F., Han Y. H. Chen, Michael A. Wulder, and Joanne C. White. 2016. “Trends in Post-Disturbance Recovery Rates of Canada’s Forests Following Wildfire and Harvest.” *Forest Ecology and Management* 361 (February): 194–207. <https://doi.org/10.1016/j.foreco.2015.11.015>.
- Baumann, Matthias, Mutlu Ozdogan, Peter T. Wolter, Alexander Krylov, Nadezda Vladimirova, and Volker C. Radeloff. 2014. “Landsat Remote Sensing of Forest Windfall Disturbance.” *Remote Sensing of Environment* 143 (March): 171–79. <https://doi.org/10.1016/j.rse.2013.12.020>.
- Belgiu, Mariana, and Lucian Drăguț. 2016. “Random Forest in Remote Sensing: A Review of Applications and Future Directions.” *ISPRS Journal of Photogrammetry and Remote Sensing* 114 (April): 24–31. <https://doi.org/10.1016/j.isprsjprs.2016.01.011>.
- Benninga, Harm-Jan F., Rogier van der Velde, and Zhongbo Su. 2019. “Impacts of Radiometric Uncertainty and Weather-Related Surface Conditions on Soil Moisture Retrievals with Sentinel-1.” *Remote Sensing* 11 (17): 2025. <https://doi.org/10.3390/rs11172025>.
- Buchhorn, Marcel, Bruno Smets, Luc Bertels, Bert De Roo, Myroslava Lesiv, Nandin-Erdene Tsendbazar, Martin Herold, and Steffen Fritz. 2020. “Copernicus Global Land Service: Land Cover 100m: Collection 3: Epoch 2017: Globe.” Zenodo. <https://doi.org/10.5281/ZENODO.3518035>.
- Calota, Iulia, Daniela Faur, and Mihai Datcu. 2022. “Estimating NDVI from SAR Images Using DNN.” In

-
- IGARSS 2022 - 2022 IEEE International Geoscience and Remote Sensing Symposium, 5232–35. <https://doi.org/10.1109/IGARSS46834.2022.9884313>.
- Carvalho, Marcela, Bertrand Le Saux, Pauline Trouvé-Peloux, Frédéric Champagnat, and Andrés Almansa. 2020. “Multitask Learning of Height and Semantics From Aerial Images.” *IEEE Geoscience and Remote Sensing Letters* 17 (8): 1391–95. <https://doi.org/10.1109/LGRS.2019.2947783>.
- César de Sá, Nuno, Mitra Baratchi, Vincent Buitenhuis, Perry Cornelissen, and Peter M. van Bodegom. 2022. “AutoML for Estimating Grass Height from ETM+/OLI Data from Field Measurements at a Nature Reserve.” *GIScience & Remote Sensing* 59 (1): 2164–83. <https://doi.org/10.1080/15481603.2022.2152304>.
- Chang, Jisung Geba, Maxim Shoshany, and Yisok Oh. 2018. “Polarimetric Radar Vegetation Index for Biomass Estimation in Desert Fringe Ecosystems.” *IEEE Transactions on Geoscience and Remote Sensing* 56 (12): 7102–8. <https://doi.org/10.1109/TGRS.2018.2848285>.
- Conrad, Felix, Mauritz Mälzer, Michael Schwarzenberger, Hajo Wiemer, and Steffen Ihlenfeldt. 2022. “Benchmarking AutoML for Regression Tasks on Small Tabular Data in Materials Design.” *Scientific Reports* 12 (1): 19350. <https://doi.org/10.1038/s41598-022-23327-1>.
- Copernicus Climate Change Service. 2019. “ERA5-Land Hourly Data from 2001 to Present.” ECMWF. <https://doi.org/10.24381/CDS.E2161BAC>.
- Dalponete, Michele, Sebastian Marzini, Yady Tatiana Solano-Correa, Giustino Tonon, Loris Vescovo, and Damiano Gianelle. 2020. “Mapping Forest Windthrows Using High Spatial Resolution Multispectral Satellite Images.” *International Journal of Applied Earth Observation and Geoinformation* 93 (December): 102206. <https://doi.org/10.1016/j.jag.2020.102206>.
- Dalponete, Michele, Yady Tatiana Solano-Correa, Daniele Marinelli, Sicong Liu, Naoto Yokoya, and Damiano Gianelle. 2023. “Detection of Forest Windthrows with Bitemporal COSMO-SkyMed and Sentinel-1 SAR Data.” *Remote Sensing of Environment* 297 (November): 113787. <https://doi.org/10.1016/j.rse.2023.113787>.
- Darra, Nicoleta, Borja Espejo-Garcia, Aikaterini Kasimati, Olga Kriezzi, Emmanouil Psomiadis, and Spyros Fountas. 2023. “Can Satellites Predict Yield? Ensemble Machine Learning and Statistical Analysis of Sentinel-2 Imagery for Processing Tomato Yield Prediction.” *Sensors* 23 (5): 2586. <https://doi.org/10.3390/s23052586>.
- Didan, Kamel. 2021a. “MODIS/Terra Vegetation Indices 16-Day L3 Global 1km SIN Grid V061.” NASA EOSDIS Land Processes Distributed Active Archive Center. <https://doi.org/10.5067/MODIS/MOD13A2.061>.
- . 2021b. “MODIS/Terra Vegetation Indices 16-Day L3 Global 250m SIN Grid V061.” NASA EOSDIS Land Processes Distributed Active Archive Center. <https://doi.org/10.5067/MODIS/MOD13Q1.061>.
- Didan, Kamel, and Armando Barreto. 2018. “VIIRS/NPP Vegetation Indices 16-Day L3 Global 500m SIN Grid V001.” NASA EOSDIS Land Processes Distributed Active Archive Center. <https://doi.org/10.5067/VIIRS/VNP13A1.001>.
- Dostalova, A., M. Milenkovic, M. Hollaus, and W. Wagner. 2016. “Influence of Forest Structure on the Sentinel-1 Backscatter Variation- Analysis with Full-Waveform LiDAR Data” 740 (August): 202.
- Dostálová, Alena, Mait Lang, Janis Ivanovs, Lars T. Waser, and Wolfgang Wagner. 2021. “European Wide Forest Classification Based on Sentinel-1 Data.” *Remote Sensing* 13 (3): 337. <https://doi.org/10.3390/rs13030337>.
- Dostálová, Alena, Wolfgang Wagner, Milutin Milenković, and Markus Hollaus. 2018. “Annual Seasonality in Sentinel-1 Signal for Forest Mapping and Forest Type Classification.” *International Journal of Remote Sensing* 39 (21): 7738–60. <https://doi.org/10.1080/01431161.2018.1479788>.
- Erickson, Nick, Jonas Mueller, Alexander Shirkov, Hang Zhang, Pedro Larroy, Mu Li, and Alexander Smola. 2020. “AutoGluon-Tabular: Robust and Accurate AutoML for Structured Data.” arXiv. <https://doi.org/10.48550/arXiv.2003.06505>.
- ESA. 2023. “Copernicus: Sentinel-1, Launches.” 2023. <https://www.eoportal.org/satellite-missions/copernicus-sentinel-1#launches>.
- Espejo-Garcia, Borja, Ioannis Malounas, Eleanna Vali, and Spyros Fountas. 2021. “Testing the Suitability of Automated Machine Learning for Weeds Identification.” *AI* 2 (1): 34–47. <https://doi.org/10.3390/ai2010004>.
- European Space Agency and Airbus. 2022. “Copernicus DEM.” European Space Agency. <https://doi.org/10.5270/ESA-c5d3d65>.
- Feurer, Matthias, Katharina Eggenberger, Stefan Falkner, Marius Lindauer, and Frank Hutter. 2022. “Auto-Sklearn 2.0: Hands-Free AutoML via Meta-Learning.” *The Journal of Machine Learning Research* 23 (1): 261:11936-261:11996.
- Feurer, Matthias, Aaron Klein, Katharina Eggenberger, Springenberg Jost, Blum Manuel, Frank Hutter, C. Cortes, et al. 2023. “Auto-Sklearn GitHub Repository.” Python. *Advances in Neural Information*

-
- Processing Systems 28 (2015)*. Curran Associates, Inc.
- Feurer, Matthias, Aaron Klein, Katharina Eggensperger, Jost Springenberg, Manuel Blum, and Frank Hutter. 2015. "Efficient and Robust Automated Machine Learning." In *Advances in Neural Information Processing Systems*. Vol. 28. Curran Associates, Inc. https://papers.nips.cc/paper_files/paper/2015/hash/11d0e6287202fced83f79975ec59a3a6-Abstract.html.
- Filgueiras, Roberto, Everardo Chartuni Mantovani, Daniel Althoff, Elpidio Inácio Fernandes Filho, and Fernando França da Cunha. 2019. "Crop NDVI Monitoring Based on Sentinel 1." *Remote Sensing* 11 (12): 1441. <https://doi.org/10.3390/rs11121441>.
- Frison, Pierre-Louis, Bénédicte Fruneau, Syrine Kmiha, Kamel Soudani, Eric Dufrêne, Thuy Le Toan, Thierry Koleck, Ludovic Villard, Eric Mougin, and Jean-Paul Rudant. 2018. "Potential of Sentinel-1 Data for Monitoring Temperate Mixed Forest Phenology." *Remote Sensing* 10 (12): 2049. <https://doi.org/10.3390/rs10122049>.
- Fuster, Beatriz, Jorge Sánchez-Zapero, Fernando Camacho, Vicente García-Santos, Aleixandre Verger, Roselyne Lacaze, Marie Weiss, Frederic Baret, and Bruno Smets. 2020. "Quality Assessment of PROBA-V LAI, FAPAR and FCOVER Collection 300 m Products of Copernicus Global Land Service." *Remote Sensing* 12 (6): 1017. <https://doi.org/10.3390/rs12061017>.
- Gamon, John A., Christopher B. Field, Michael L. Goulden, Kevin L. Griffin, Anne E. Hartley, Geeske Joel, Josep Penuelas, and Riccardo Valentini. 1995. "Relationships Between NDVI, Canopy Structure, and Photosynthesis in Three Californian Vegetation Types." *Ecological Applications* 5 (1): 28–41. <https://doi.org/10.2307/1942049>.
- García-Llamas, Paula, Susana Suárez-Seoane, José Manuel Fernández-Guisuraga, Víctor Fernández-García, Alfonso Fernández-Manso, Carmen Quintano, Angela Taboada, Elena Marcos, and Leonor Calvo. 2019. "Evaluation and Comparison of Landsat 8, Sentinel-2 and Deimos-1 Remote Sensing Indices for Assessing Burn Severity in Mediterranean Fire-Prone Ecosystems." *International Journal of Applied Earth Observation and Geoinformation* 80 (August): 137–44. <https://doi.org/10.1016/j.jag.2019.04.006>.
- Hänsch, Ronny, Claudio Persello, Gemine Vivone, Javiera Castillo Navarro, Alexandre Boulch, Sebastien Lefevre, and Bertrand Le Saux. 2022. "Report on the 2022 IEEE Geoscience and Remote Sensing Society Data Fusion Contest: Semisupervised Learning [Technical Committees]." *IEEE Geoscience and Remote Sensing Magazine* 10 (4): 270–73. <https://doi.org/10.1109/MGRS.2022.3219935>.
- Hansen, M. C., P. V. Potapov, R. Moore, M. Hancher, S. A. Turubanova, A. Tyukavina, D. Thau, et al. 2013. "High-Resolution Global Maps of 21st-Century Forest Cover Change." *Science* 342 (6160): 850–53. <https://doi.org/10.1126/science.1244693>.
- Hird, Jennifer N., Evan R. DeLancey, Gregory J. McDermid, and Jahan Kariyeva. 2017. "Google Earth Engine, Open-Access Satellite Data, and Machine Learning in Support of Large-Area Probabilistic Wetland Mapping." *Remote Sensing* 9 (12): 1315. <https://doi.org/10.3390/rs9121315>.
- Hlásny, Tomáš, Louis König, Paal Krokene, Marcus Lindner, Claire Montagné-Huck, Jörg Müller, Hua Qin, et al. 2021. "Bark Beetle Outbreaks in Europe: State of Knowledge and Ways Forward for Management." *Current Forestry Reports* 7 (3): 138–65. <https://doi.org/10.1007/s40725-021-00142-x>.
- Hollmann, Noah, Samuel Müller, Katharina Eggensperger, and Frank Hutter. 2023. "TabPFN: A Transformer That Solves Small Tabular Classification Problems in a Second." arXiv. <https://doi.org/10.48550/arXiv.2207.01848>.
- Holtgrave, Ann-Kathrin, Norbert Röder, Andrea Ackermann, Stefan Erasmi, and Birgit Kleinschmit. 2020. "Comparing Sentinel-1 and -2 Data and Indices for Agricultural Land Use Monitoring." *Remote Sensing* 12 (18): 2919. <https://doi.org/10.3390/rs12182919>.
- Huang, Sha, Lina Tang, Joseph P. Hupy, Yang Wang, and Guofan Shao. 2021. "A Commentary Review on the Use of Normalized Difference Vegetation Index (NDVI) in the Era of Popular Remote Sensing." *Journal of Forestry Research* 32 (1): 1–6. <https://doi.org/10.1007/s11676-020-01155-1>.
- Huete, A, K Didan, T Miura, E. P Rodriguez, X Gao, and L. G Ferreira. 2002. "Overview of the Radiometric and Biophysical Performance of the MODIS Vegetation Indices." *Remote Sensing of Environment, The Moderate Resolution Imaging Spectroradiometer (MODIS): a new generation of Land Surface Monitoring*, 83 (1): 195–213. [https://doi.org/10.1016/S0034-4257\(02\)00096-2](https://doi.org/10.1016/S0034-4257(02)00096-2).
- Hutter, Frank, Holger H. Hoos, and Kevin Leyton-Brown. 2011. "Sequential Model-Based Optimization for General Algorithm Configuration." In *Learning and Intelligent Optimization*, edited by Carlos A. Coello Coello, 507–23. Lecture Notes in Computer Science. Berlin, Heidelberg: Springer. https://doi.org/10.1007/978-3-642-25566-3_40.
- Jiao, Xianfeng, Heather McNairn, and Laura Dingle Robertson. 2021. "Monitoring Crop Growth Using a Canopy Structure Dynamic Model and Time Series of Synthetic Aperture Radar (SAR) Data." *International Journal of Remote Sensing* 42 (17): 6433–60.

-
- <https://doi.org/10.1080/01431161.2021.1938739>.
- Jin, Haifeng, François Chollet, Qingquan Song, and Xia Hu. 2023. “AutoKeras: An AutoML Library for Deep Learning.” *Journal of Machine Learning Research* 24 (6): 1–6.
- Kaiser, Philipp, Henning Buddenbaum, Sascha Nink, and Joachim Hill. 2022. “Potential of Sentinel-1 Data for Spatially and Temporally High-Resolution Detection of Drought Affected Forest Stands.” *Forests* 13 (12): 2148. <https://doi.org/10.3390/f13122148>.
- Kasimati, Aikaterini, Borja Espejo-García, Nicoleta Darra, and Spyros Fountas. 2022. “Predicting Grape Sugar Content under Quality Attributes Using Normalized Difference Vegetation Index Data and Automated Machine Learning.” *Sensors* 22 (9): 3249. <https://doi.org/10.3390/s22093249>.
- Kiala, Zolo, Onesimo Mutanga, John Odindi, Kabir Y Peerbhay, and Rob Slotow. 2020. “Automated Classification of a Tropical Landscape Infested by Parthenium Weed (Parthenium Hyterophorus).” *International Journal of Remote Sensing* 41 (22): 8497–8519. <https://doi.org/10.1080/01431161.2020.1779375>.
- Kim, Y., and J. van Zyl. 2000. “On the Relationship between Polarimetric Parameters.” In *IGARSS 2000. IEEE 2000 International Geoscience and Remote Sensing Symposium. Taking the Pulse of the Planet: The Role of Remote Sensing in Managing the Environment. Proceedings (Cat. No.00CH37120)*, 3:1298–1300. Honolulu, HI, USA: IEEE. <https://doi.org/10.1109/IGARSS.2000.858099>.
- Kosztra, Barbara, György Büttner, Gerard Hazeu, and Stephan Arnold. 2019. “Updated CLC Illustrated Nomenclature Guidelines.” European Environment Agency. https://land.copernicus.eu/user-corner/technical-library/corine-land-cover-nomenclature-guidelines/docs/pdf/CLC2018_Nomenclature_illustrated_guide_20190510.pdf.
- Langanke, Tobias. 2017. “Copernicus Land Monitoring Service – High Resolution Layer Forest: Product Specifications Document.” Copernicus team at EEA. <https://land.copernicus.eu/en/technical-library/hrl-forest-2012-2015/@@@download/file>.
- Lasko, Kristofer. 2022. “Gap Filling Cloudy Sentinel-2 NDVI and NDWI Pixels with Multi-Frequency Denoised C-Band and L-Band Synthetic Aperture Radar (SAR), Texture, and Shallow Learning Techniques.” *Remote Sensing* 14 (17): 4221. <https://doi.org/10.3390/rs14174221>.
- Lastovicka, Josef, Pavel Svec, Daniel Paluba, Natalia Kobliuk, Jan Svoboda, Radovan Hladky, and Premysl Stych. 2020. “Sentinel-2 Data in an Evaluation of the Impact of the Disturbances on Forest Vegetation.” *Remote Sensing* 12 (12): 1914. <https://doi.org/10.3390/rs12121914>.
- Lee, Jong-Sen. 1985. “Speckle Suppression and Analysis for Synthetic Aperture Radar Images.” In *Intl Conf on Speckle*, 0556:170–79. SPIE. <https://doi.org/10.1117/12.949537>.
- Liu, Hui Qing, and Alfredo Huete. 1995. “A Feedback Based Modification of the NDVI to Minimize Canopy Background and Atmospheric Noise.” *IEEE Transactions on Geoscience and Remote Sensing* 33 (2): 457–65. <https://doi.org/10.1109/TGRS.1995.8746027>.
- Mandal, Dipankar, Vineet Kumar, Debanshu Ratha, Subhadip Dey, Avik Bhattacharya, Juan M. Lopez-Sanchez, Heather McNairn, and Yalamanchili S. Rao. 2020. “Dual Polarimetric Radar Vegetation Index for Crop Growth Monitoring Using Sentinel-1 SAR Data.” *Remote Sensing of Environment* 247 (September): 111954. <https://doi.org/10.1016/j.rse.2020.111954>.
- Mandal, Dipankar, Debanshu Ratha, Avik Bhattacharya, Vineet Kumar, Heather McNairn, Yalamanchili S. Rao, and Alejandro C. Frery. 2020. “A Radar Vegetation Index for Crop Monitoring Using Compact Polarimetric SAR Data.” *IEEE Transactions on Geoscience and Remote Sensing* 58 (9): 6321–35. <https://doi.org/10.1109/TGRS.2020.2976661>.
- Marinelli, Daniele, Michele Dalponte, Lorenzo Frizzera, Erik Næsset, and Damiano Gianelle. 2023. “A Method for Continuous Sub-Annual Mapping of Forest Disturbances Using Optical Time Series.” *Remote Sensing of Environment* 299 (December): 113852. <https://doi.org/10.1016/j.rse.2023.113852>.
- Mazza, Antonio, Massimiliano Gargiulo, Giuseppe Scarpa, and Raffaele Gaetano. 2018. “Estimating the NDVI from SAR by Convolutional Neural Networks.” In *IGARSS 2018 - 2018 IEEE International Geoscience and Remote Sensing Symposium*, 1954–57. <https://doi.org/10.1109/IGARSS.2018.8519459>.
- McMahon, Sean M., Geoffrey G. Parker, and Dawn R. Miller. 2010. “Evidence for a Recent Increase in Forest Growth.” *Proceedings of the National Academy of Sciences* 107 (8): 3611–15. <https://doi.org/10.1073/pnas.0912376107>.
- Ministry of Agriculture of the Czech Republic. 2022. “Information on Forests and Forestry in the Czech Republic by 2021.” Ministry of Agriculture of the Czech Republic. https://eagri.cz/public/web/file/719202/Zprava_o_stavu_lesa_2021_ENG_web.pdf.
- Mohite, J. D., S. A. Sawant, A. Pandit, and S. Pappula. 2020. “INVESTIGATING THE PERFORMANCE OF RANDOM FOREST AND SUPPORT VECTOR REGRESSION FOR ESTIMATION OF CLOUD-FREE NDVI USING SENTINEL-1 SAR DATA.” *The International Archives of the Photogrammetry, Remote Sensing and Spatial Information Sciences XLIII-B3-2020* (August): 1379–83. <https://doi.org/10.5194/isprs-archives-XLIII-B3-2020-1379-2020>.

-
- Moran, M. Susan, Luis Alonso, Jose F. Moreno, Maria Pilar Cendrero Mateo, D. Fernando de la Cruz, and Amelia Montoro. 2012. "A RADARSAT-2 Quad-Polarized Time Series for Monitoring Crop and Soil Conditions in Barrax, Spain." *IEEE Transactions on Geoscience and Remote Sensing* 50 (4): 1057–70. <https://doi.org/10.1109/TGRS.2011.2166080>.
- Myneni, Ranga, and Yuri Knyazikhin. 2018. "VIIRS/NPP Leaf Area Index/FPAR 8-Day L4 Global 500m SIN Grid V001." NASA EOSDIS Land Processes Distributed Active Archive Center. <https://doi.org/10.5067/VIIRS/VNP15A2H.001>.
- Myneni, Ranga, Yuri Knyazikhin, and Taejin Park. 2021. "MODIS/Terra+Aqua Leaf Area Index/FPAR 4-Day L4 Global 500m SIN Grid V061." NASA EOSDIS Land Processes Distributed Active Archive Center. <https://doi.org/10.5067/MODIS/MCD15A3H.061>.
- Naik, Parth, Michele Dalponte, and Lorenzo Bruzzone. 2023. "Automated Machine Learning Driven Stacked Ensemble Modeling for Forest Aboveground Biomass Prediction Using Multitemporal Sentinel-2 Data." *IEEE Journal of Selected Topics in Applied Earth Observations and Remote Sensing* 16: 3442–54. <https://doi.org/10.1109/JSTARS.2022.3232583>.
- Olesk, Aire, Kaupo Voormansik, Mirjam Põhjala, and Mart Noorma. 2015. "Forest Change Detection from Sentinel-1 and ALOS-2 Satellite Images." In *2015 IEEE 5th Asia-Pacific Conference on Synthetic Aperture Radar (APSAR)*, 522–27. <https://doi.org/10.1109/APSAR.2015.7306263>.
- Olson, Randal S., and Jason H. Moore. 2019. "TPOT: A Tree-Based Pipeline Optimization Tool for Automating Machine Learning." In *Automated Machine Learning: Methods, Systems, Challenges*, edited by Frank Hutter, Lars Kotthoff, and Joaquin Vanschoren, 151–60. The Springer Series on Challenges in Machine Learning. Cham: Springer International Publishing. https://doi.org/10.1007/978-3-030-05318-5_8.
- Palacios Salinas, Nelly Rosaura, Mitra Baratchi, Jan N. van Rijn, and Andreas Vollrath. 2021. "Automated Machine Learning for Satellite Data: Integrating Remote Sensing Pre-Trained Models into AutoML Systems." In *Machine Learning and Knowledge Discovery in Databases. Applied Data Science Track*, edited by Yuxiao Dong, Nicolas Kourtellis, Barbara Hammer, and Jose A. Lozano, 447–62. Lecture Notes in Computer Science. Cham: Springer International Publishing. https://doi.org/10.1007/978-3-030-86517-7_28.
- Paluba, Daniel, Josef Laštovička, Antonios Mouratidis, and Přemysl Štych. 2021. "Land Cover-Specific Local Incidence Angle Correction: A Method for Time-Series Analysis of Forest Ecosystems." *Remote Sensing* 13 (9): 1743. <https://doi.org/10.3390/rs13091743>.
- Paluba, Daniel, Lorenzo Giuliano Papale, Triantafyllia-Maria Perivolioti, Přemysl Štych, Josef Laštovička, Panagiotis Kalaitzis, Georgia Karadimou, Elena Papageorgiou, and Antonios Mouratidis. 2023. "Unsupervised Burned Area Mapping in Greece: Investigating the Impact of Precipitation, Pre- and Post-Processing of Sentinel-1 Data in Google Earth Engine." In *IGARSS 2023 - 2023 IEEE International Geoscience and Remote Sensing Symposium*, 2520–23. <https://doi.org/10.1109/IGARSS52108.2023.10283130>.
- Pan, Yude, Richard A. Birdsey, Jingyun Fang, Richard Houghton, Pekka E. Kauppi, Werner A. Kurz, Oliver L. Phillips, et al. 2011. "A Large and Persistent Carbon Sink in the World's Forests." *Science* 333 (6045): 988–93. <https://doi.org/10.1126/science.1201609>.
- Pedregosa, Fabian, Gaël Varoquaux, Alexandre Gramfort, Vincent Michel, Bertrand Thirion, Olivier Grisel, Mathieu Blondel, et al. 2011. "Scikit-Learn: Machine Learning in Python." *Journal of Machine Learning Research* 12 (85): 2825–30.
- Periasamy, Shoba. 2018. "Significance of Dual Polarimetric Synthetic Aperture Radar in Biomass Retrieval: An Attempt on Sentinel-1." *Remote Sensing of Environment* 217 (November): 537–49. <https://doi.org/10.1016/j.rse.2018.09.003>.
- Pinheiro, Muriel, Nuno Miranda, Andrea Recchia, Alessandro Cotrufo, Niccolo Franceschi, Riccardo Piantanida, Kersten Schmidt, Christoph Gisinger, Guillaume Hajduch, and Pauline Vincent. 2022. "Sentinel-1 Instruments Status and Product Performance Update for 2022." In *EUSAR 2022: 14th European Conference on Synthetic Aperture Radar*, 1–5.
- Quintano, C., A. Fernández-Manso, and O. Fernández-Manso. 2018. "Combination of Landsat and Sentinel-2 MSI Data for Initial Assessing of Burn Severity." *International Journal of Applied Earth Observation and Geoinformation* 64 (February): 221–25. <https://doi.org/10.1016/j.jag.2017.09.014>.
- Ranson, K.J., and G. Sun. 2000. "Effects of Environmental Conditions on Boreal Forest Classification and Biomass Estimates with SAR." *IEEE Transactions on Geoscience and Remote Sensing* 38 (3): 1242–52. <https://doi.org/10.1109/36.843016>.
- Reiche, Johannes, Adugna Mullissa, Bart Slagter, Yaqing Gou, Nandin-Erdene Tsendbazar, Christelle Odongo-Braun, Andreas Vollrath, et al. 2021. "Forest Disturbance Alerts for the Congo Basin Using Sentinel-1." *Environmental Research Letters* 16 (2): 024005. <https://doi.org/10.1088/1748-9326/abd0a8>.
- Renza, Diego, Elsa Adriana Cárdenas, Carlos Marcelo Jaramillo, Serena Sarah Weber, and Estibaliz Martinez.

2021. "Landslide Susceptibility Model by Means of Remote Sensing Images and AutoML." In *Applied Computer Sciences in Engineering*, edited by Juan Carlos Figueroa-García, Yesid Díaz-Gutierrez, Elvis Eduardo Gaona-García, and Alvaro David Orjuela-Cañón, 25–37. Communications in Computer and Information Science. Cham: Springer International Publishing.
https://doi.org/10.1007/978-3-030-86702-7_3.
- Richards, John A. 2009. "The Imaging Radar System." In *Remote Sensing with Imaging Radar*, edited by John A. Richards, 1–10. Signals and Communication Technology. Berlin, Heidelberg: Springer.
https://doi.org/10.1007/978-3-642-02020-9_1.
- Roßberg, Thomas, and Michael Schmitt. 2022. "Estimating NDVI from Sentinel-1 Sar Data Using Deep Learning." In *IGARSS 2022 - 2022 IEEE International Geoscience and Remote Sensing Symposium*, 1412–15. <https://doi.org/10.1109/IGARSS46834.2022.9883707>.
- . 2023. "A Globally Applicable Method for NDVI Estimation from Sentinel-1 SAR Backscatter Using a Deep Neural Network and the SEN12TP Dataset." *PFG – Journal of Photogrammetry, Remote Sensing and Geoinformation Science* 91 (3): 171–88. <https://doi.org/10.1007/s41064-023-00238-y>.
- Rüetschi, Marius, David Small, and Lars Waser. 2019. "Rapid Detection of Windthrows Using Sentinel-1 C-Band SAR Data." *Remote Sensing* 11 (2): 115. <https://doi.org/10.3390/rs11020115>.
- Saatchi, Sasan. 2019. "SAR Methods for Mapping and Monitoring Forest Biomass." In *SAR Handbook: Comprehensive Methodologies for Forest Monitoring and Biomass Estimation*. NASA.
<https://gis1.servirglobal.net/TrainingMaterials/SAR/ch5.pdf>.
- Sahadevan, DINESH KUMAR, Srinivasa Sitiraju, and Jaswant Sharma. 2013. *Radar Vegetation Index as an Alternative to NDVI for Monitoring of Soyabean and Cotton*.
- Santos, Erli Pinto dos, Demetrius David Da Silva, and Cibele Hummel do Amaral. 2021. "Vegetation Cover Monitoring in Tropical Regions Using SAR-C Dual-Polarization Index: Seasonal and Spatial Influences." *International Journal of Remote Sensing* 42 (19): 7581–7609.
<https://doi.org/10.1080/01431161.2021.1959955>.
- Santos, Erli Pinto dos, Demetrius David da Silva, Cibele Hummel do Amaral, Elpídio Inácio Fernandes-Filho, and Rafael Luís Silva Dias. 2022. "A Machine Learning Approach to Reconstruct Cloudy Affected Vegetation Indices Imagery via Data Fusion from Sentinel-1 and Landsat 8." *Computers and Electronics in Agriculture* 194 (March): 106753. <https://doi.org/10.1016/j.compag.2022.106753>.
- Schellenberg, Konstantin, Thomas Jagdhuber, Markus Zehner, Sören Hese, Marcel Urban, Mikhail Urbazaev, Henrik Hartmann, Christiane Schmillius, and Clémence Dubois. 2023. "Potential of Sentinel-1 SAR to Assess Damage in Drought-Affected Temperate Deciduous Broadleaf Forests." *Remote Sensing* 15 (4): 1004. <https://doi.org/10.3390/rs15041004>.
- Schmitt, Michael, Seyed Ali Ahmadi, Yonghao Xu, Gülşen Taşkin, Ujjwal Verma, Francescopaolo Sica, and Ronny Hänsch. 2023. "There Are No Data Like More Data: Datasets for Deep Learning in Earth Observation." *IEEE Geoscience and Remote Sensing Magazine* 11 (3): 63–97.
<https://doi.org/10.1109/MGRS.2023.3293459>.
- scikit-learn. 2023. "Sklearn.Ensemble.RandomForestRegressor." Scikit-Learn. 2023.
<https://scikit-learn/stable/modules/generated/sklearn.ensemble.RandomForestRegressor.html>.
- Smets, Bruno, Zhanzhang Cai, Lars Elkund, Feng Tian, Kasper Bonte, Roel Van Hoost, Ruben Van De Kerchove, et al. 2023. "High Resolution Vegetation Phenology and Productivity (HR-VPP), Daily Raw Vegetation Indices." European Union, Copernicus Land Monitoring Service 2021, European Environment Agency (EEA).
<https://land.copernicus.eu/en/technical-library/algorithm-theoretical-base-document-for-vegetation-indices/@@download/file>.
- Stych, Premysl, Josef Lastovicka, Radovan Hladky, and Daniel Paluba. 2019. "Evaluation of the Influence of Disturbances on Forest Vegetation Using the Time Series of Landsat Data: A Comparison Study of the Low Tatras and Sumava National Parks." *ISPRS International Journal of Geo-Information* 8 (2): 71.
<https://doi.org/10.3390/ijgi8020071>.
- Thornton, Chris, Frank Hutter, Holger H. Hoos, and Kevin Leyton-Brown. 2013. "Auto-WEKA: Combined Selection and Hyperparameter Optimization of Classification Algorithms." arXiv.
<https://doi.org/10.48550/arXiv.1208.3719>.
- Tornede, Tanja, Alexander Tornede, Jonas Hanselle, Felix Mohr, Marcel Wever, and Eyke Hüllermeier. 2023. "Towards Green Automated Machine Learning: Status Quo and Future Directions." *Journal of Artificial Intelligence Research* 77 (June): 427–57. <https://doi.org/10.1613/jair.1.14340>.
- Tuia, Devis, Gabriele Moser, Bertrand Le Saux, Benjamin Bechtel, and Linda See. 2017. "2017 IEEE GRSS Data Fusion Contest: Open Data for Global Multimodal Land Use Classification [Technical Committees]." *IEEE Geoscience and Remote Sensing Magazine* 5 (1): 70–73.
<https://doi.org/10.1109/MGRS.2016.2645380>.
- Tuia, Devis, Konrad Schindler, Begüm Demir, Gustau Camps-Valls, Xiao Xiang Zhu, Mrinalini Kochupillai,

- Sašo Džeroski, et al. 2023. “Artificial Intelligence to Advance Earth Observation: A Perspective.” arXiv. <https://doi.org/10.48550/arXiv.2305.08413>.
- Van Tricht, Kristof. 2023. “Kvantricht/Gee-Biopar: Gee-Biopar v1.0.0.” Zenodo. <https://doi.org/10.5281/ZENODO.10103928>.
- Vreugdenhil, Mariette, Wolfgang Wagner, Bernhard Bauer-Marschallinger, Isabella Pfeil, Irene Teubner, Christoph Rüdiger, and Peter Strauss. 2018. “Sensitivity of Sentinel-1 Backscatter to Vegetation Dynamics: An Austrian Case Study.” *Remote Sensing* 10 (9): 1396. <https://doi.org/10.3390/rs10091396>.
- Weiss, Marie, and Frederic Baret. 2016. “S2ToolBox Level 2 Products: LAI, FAPAR, FCOVER. Version 1.1.” http://step.esa.int/docs/extra/ATBD_S2ToolBox_L2B_V1.1.pdf.
- WMO, Scientific and Cultural Organization (UNESCO) United Nations Educational, United Nations Environment Programme (UNEP), and International Council for Science (ICSU). 2011. “Systematic Observation Requirements for Satellite-Based Products for Climate Supplemental Details to the Satellite-Based Component of the Implementation Plan for the Global Observing System for Climate in Support of the UNFCCC.” 2011. <https://library.wmo.int/records/item/48411-systematic-observation-requirements-for-satellite-based-products-for-climate-supplemental-details-to-the-satellite-based-component-of-the-implementation-plan-for-the-global-observing-system-for-climate-in-support-of-the-unfccc>.
- Zanaga, Daniele, Ruben Van De Kerchove, Dirk Daems, Wanda De Keersmaecker, Carsten Brockmann, Grit Kirches, Jan Wevers, et al. 2022. “ESA WorldCover 10 m 2021 V200.” Zenodo. <https://doi.org/10.5281/ZENODO.7254221>.
- Zupanc, Anze. 2017. “Improving Cloud Detection with Machine Learning.” *Sentinel Hub Blog* (blog). December 19, 2017. <https://medium.com/sentinel-hub/improving-cloud-detection-with-machine-learning-c09dc5d7cf13>.

Appendices

Appendix I. Auto-sklearn regressors, feature and data preprocessors with the number of their hyperparameters ($\# \lambda$). Based on the source-code of auto-sklearn on GitHub (Feurer et al. 2023) [accessed on 26.09.2023].

Regressor	$\# \lambda$	Feature preprocessor	$\# \lambda$	Data preprocessor	$\# \lambda$
adaboost	4	densifier	-	Cat. encoder	3
ard_regression	8	Extra Trees Regr. Prep.	9	imputation	2
decision_tree	8	fast ICA	4	Category Shift	-
extra_trees	9	feature agglomeration	4	rescaling	10
gaussian_process	3	kernel PCA	5	Cat. minority coalescer	2
gradient_boosting	12	Random Kitchen Sinks	2		
k_nearest_neighbors	3	linear SVM prepr.	3		
liblinear_svr	4	no preprocessing	-		
libsvm_svr	7	Nystroem kernel approx.	5		
mlp	15	PCA	2		
random_forest	9	Polynomial Features	3		
sgd	11	Random Trees Embedding	7		
		select perc. Regression	2		
		Univariate Feature Selection based on rates	3		
		truncatedSVD	1		